TIME-DOMAIN FULL-WAVE MODELING OF NONLINEAR AIR BREAKDOWN IN HIGH-POWER MICROWAVE DEVICES AND SYSTEMS

Su Yan and
Jian-Ming Jin

Center for Computational Electromagnetics
Department of Electrical and Computer Engineering
University of Illinois
Urbana, IL 61801

30 September 2017

Final Report

APPROVED FOR PUBLIC RELEASE: DISTRIBUTION IS UNLIMITED.

AIR FORCE RESEARCH LABORATORY
Directed Energy Directorate
3550 Aberdeen Ave SE
AIR FORCE MATERIEL COMMAND
KIRTLAND AIR FORCE BASE, NM 87117-5776

NOTICE AND SIGNATURE PAGE

AFRL-RD-PS-TR-2017-0047 HAS BEEN REVIEWED AND IS APPROVED FOR PUBLICATION IN ACCORDANCE WITH ASSIGNED DISTRIBUTION STATEMENT.

_____   _____
ANDREW GREENWOOD, DR-IV   PETER MARDAHL, DR-IV
Program Manager   Technical Advisor, Modeling and Effects

REPORT DOCUMENTATION PAGE

Public reporting burden for this collection of information is estimated to average 1 hour per response, including the time for reviewing instructions, searching existing data sources, gathering and maintaining the data needed, and completing and reviewing this collection of information. Send comments regarding this burden estimate or any other aspect of this collection of information, including suggestions for reducing this burden to Department of Defense, Washington Headquarters Services, Directorate for Information Operations and Reports (0704-0188), 1215 Jefferson Davis Highway, Suite 1204, Arlington, VA 22202-4302. Respondents should be aware that notwithstanding any other provision of law, no person shall be subject to any penalty for failing to comply with a collection of information if it does not display a currently valid OMB control number. **PLEASE DO NOT RETURN YOUR FORM TO THE ABOVE ADDRESS.**

1. REPORT DATE *(DD-MM-YYYY)* 30-09-2017	2. REPORT TYPE Final Report		3. DATES COVERED *(From - To)* 31-08-2016 – 31-08-2017
4. TITLE AND SUBTITLE Time-Domain Full-Wave Modeling of Nonlinear Air Breakdown in High-Power Microwave Devices and Systems			**5a. CONTRACT NUMBER**
			5b. GRANT NUMBER FA9451-16-1-0051
			5c. PROGRAM ELEMENT NUMBER 62605F
6. AUTHOR(S) Su Yan and Jian-Ming Jin			**5d. PROJECT NUMBER** 4867NSAA
			5e. TASK NUMBER EF127830
			5f. WORK UNIT NUMBER D09L
7. PERFORMING ORGANIZATION NAME(S) AND ADDRESS(ES) Center for Computational Electromagnetics Department of Electrical and Computer Engineering University of Illinois Urbana, IL 61801			**8. PERFORMING ORGANIZATION REPORT NUMBER**
9. SPONSORING / MONITORING AGENCY NAME(S) AND ADDRESS(ES) Air Force Research Laboratory 3550 Aberdeen Avenue SE Kirtland AFB, NM 87117-5776			**10. SPONSOR/MONITOR'S ACRONYM(S)** AFRL/RDHE
			11. SPONSOR/MONITOR'S REPORT NUMBER(S) AFRL-RD-PS-TR-2017-0047

12. DISTRIBUTION / AVAILABILITY STATEMENT
Approved for public release; distribution is unlimited.

13. SUPPLEMENTARY NOTES

14. ABSTRACT
This final report describes the effort to develop a discontinuous Galerkin time-domain (DGTD) method in the simulation of high-power microwave air breakdown phenomena, which are modeled by a coupled electromagnetic--plasma system. In the coupled system, the electromagnetic fields are governed by Maxwell's equations and the plasma is modeled by the five-moment fluid equations (Euler's equations). The non-Maxwellian electron energy distribution function (EEDF) is used to calculate electron transport coefficients and describe the non-equilibrium collision reactions between electrons and neutral air particles. The coupled Maxwell--Euler equations are solved by the DGTD method with high-order spatial and temporal discretizations, which are able to provide a sufficient resolution for the physical quantities in both space and time. Several numerical examples are presented to investigate the physical process and demonstrate the capability of the numerical method.

15. SUBJECT TERMS
High power microwave, time-domain, finite-element, discontinuous-Galerkin, nonlinear breakdown

16. SECURITY CLASSIFICATION OF:			17. LIMITATION OF ABSTRACT	18. NUMBER OF PAGES	19a. NAME OF RESPONSIBLE PERSON Andrew Greenwood
a. REPORT UNCLASSIFIED	**b. ABSTRACT** UNCLASSIFIED	**c. THIS PAGE** UNCLASSIFIED	SAR	42	**19b. TELEPHONE NUMBER** *(include area code)* (505) 846-6642

TABLE OF CONTENTS

Section   **Page**

LIST OF FIGURES

Figure   **Page**

LIST OF TABLES

1.0 SUMMARY

In this report, a discontinuous Galerkin time-domain (DGTD) method is developed to simulate high-power microwave (HPM) air breakdown phenomena, which are modeled by a coupled electromagnetic--plasma system. In the coupled system, the electromagnetic fields are governed by Maxwell's equations and the plasma is modeled by the five-moment fluid equations (Euler's equations). The non-Maxwellian electron energy distribution function (EEDF) is used to calculate electron transport coefficients and describe the non-equilibrium collision reactions between electrons and neutral air particles. The coupled Maxwell--Euler equations are solved by the DGTD method with high-order spatial and temporal discretizations, which are able to provide a sufficient resolution for the physical quantities in both space and time. Several numerical examples are presented to investigate the physical process and demonstrate the capability of the numerical method.

2.0 INTRODUCTION

When HPM pulses travel through air, the high energy of the pulses can ionize neutral air particles and cause air to break down. In this process, a huge number of free electrons are generated and heated up by the power supplied by the electromagnetic fields. The electron oscillation generates secondary fields which, when strong enough, can cancel a part of the HPM pulses being transmitted and cause the so-called HPM tail erosion and pulse shortening. This will severely limit the transmission of the HPM pulses in air and has been investigated by many researchers [1]-[11].

To describe the HPM breakdown process, different models can be employed. Based on the fact of the insulator-to-conductor transition during breakdown, a nonlinear conductivity model was developed in [12], where the material conductivity was assumed to be a nonlinear function of the electric field. In [13], a simplified plasma model considering particle collisions was employed. In this model, the plasma velocity was treated as an unknown quantity governed by the momentum transfer equation with collision. The resulting coupled system was solved by a nonlinear finite-element time-domain (FETD) method. To include more physics, a plasma diffusion model was adopted and solved by a coupled DGTD method in [14], where the air breakdown and tail erosion were simulated by considering both the electron density and velocity as unknown quantities. To obtain a numerical solution with a higher fidelity, a five-moment plasma fluid model is adopted in this work, where the plasma density, velocity, and energy are all considered and described by three conservation laws obtained by taking the first three moments of the Boltzmann equation. To describe the non-equilibrium collision process between electrons and neutral particles, the transport coefficients are calculated by integrating the collision cross sections with the non-Maxwellian EEDF [9], [15].

In the simulation of the coupled electromagnetic--plasma system, the finite-difference time-domain (FDTD) method [11], [16] is most widely used because of its simplicity and high parallel efficiency. However, the stair-case approximation of the solution domain, the finite difference approximation of the fields and their derivatives, and the explicit leap-frog time-marching scheme used in the FDTD method result in an overall low-order accuracy, which requires an extremely dense mesh grid and an extremely tiny time step size in a simulation to achieve a desired accuracy. To overcome these issues, a coupled high-order DGTD scheme [17]-[21] is adopted in this report

to solve the coupled system equations. Using an unstructured mesh, high-order nodal basis functions and an explicit high-order time-marching scheme, the employed DGTD method is able to achieve a high-order accuracy in the spatial and temporal representations of the physical quantities. Also, it is able to preserve the continuity of all components of the electromagnetic fields due to the application of the nodal basis functions [22], which is critical in maintaining the stability of a Boltzmann solver. Moreover, the flexibility and efficiency of the DGTD method can be enhanced through the application of the dynamic *h*- and/or *p*-adaptation techniques [23], [24] and massive parallelization on a multi-core CPU cluster or a many-core graphic processing unit (GPU) platform [25], [26].

This report is organized as follows. In Section 3.0, the five-moment fluid model is first introduced, followed by the description of the calculation of its source terms. The DGTD solution of the coupled Maxwell--Euler system is then presented. The electromagnetic--plasma interactions and the resulting air breakdown, electromagnetic pulse tail erosion, plasma formation and shielding are simulated and given as numerical examples in Section 4.0 to demonstrate the physical process and validate the numerical method. Conclusions are drawn in Section 5.0. Note that in this report, only electrons are considered. The positive and negative ions are considered as immobile due to their large mass and therefore, the ion currents and their radiation are neglected.

3.0 METHODS, ASSUMPTIONS, AND PROCEDURES

3.1 Plasma Model

3.1.1 The Boltzmann & General Transport Equations

The behaviors of electrons are governed by the Boltzmann equation [27]-[30], which reads

$$\frac{\partial f}{\partial t} + \boldsymbol{v} \cdot \nabla f + \frac{\boldsymbol{F}}{m_{\mathrm{e}}} \cdot \nabla_v f = \left(\frac{\partial f}{\partial t}\right)_{\mathrm{coll}} \tag{1}$$

where $f = f(\boldsymbol{r}, \boldsymbol{v}, t)$ denotes the electron distribution function defined in the seven-dimensional phase space $(\boldsymbol{r}, \boldsymbol{v}, t)$, m_{e} denotes the electron mass at rest, and $\boldsymbol{F}$ denotes the macroscopic force such as the electromagnetic (Lorentz) and gravitational forces. In the rest of this report, $\boldsymbol{F}$ denotes the Lorentz force only, since the gravitational force is negligible when comparing with the Lorentz force in problems considered here. The operators ∇ and $\nabla_{\boldsymbol{v}}$ denote the gradients taken in the physical space $\boldsymbol{r} = (x, y, z)$ and the velocity space $\boldsymbol{v} = (v_x, v_y, v_z)$, respectively. The right-hand side (RHS) of the Boltzmann equation is an abstract form representing the temporal variation of the electron distribution function due to collisions.

In fluid models, the behaviors of various discharge particle species are described in terms of average, macroscopic, hydrodynamic quantities such as the particle density

$$n(\boldsymbol{r}, t) = \int f(\boldsymbol{r}, \boldsymbol{v}, t) \, \mathrm{d}\boldsymbol{v} \tag{2}$$

the mean velocity

2

$$U(r,t) = \langle v \rangle = \frac{1}{n} \int v f(r,v,t) \, dv \tag{3}$$

and the mean energy

$$\mathcal{E}(r,t) = \frac{1}{2} m_{\mathrm{e}} \langle v^2 \rangle = \frac{m_{\mathrm{e}}}{2n} \int v^2 f(r,v,t) \, dv \tag{4}$$

In general, a macroscopically averaged quantity can be defined as

$$\langle \Phi(v) \rangle = \frac{1}{n} \int \Phi(v) \, f(r,v,t) \, dv = \frac{\int \Phi(v) \, f(r,v,t) \, dv}{\int f(r,v,t) \, dv} \tag{5}$$

where Φ is some function of velocity, which can be a scalar, a vector, or a tensor. In (3) and (4), Φ are taken as the microscopic velocity v and the microscopic energy $\frac{1}{2} m_{\mathrm{e}} v^2$ of a single electron, respectively.

Multiplying the Boltzmann equation by $\Phi(v)$ and integrating over all velocity components yield the general transport equation

$$\int \Phi(v) \, \frac{\partial f}{\partial t} \, dv + \int \Phi(v) \, v \cdot \nabla f \, dv + \int \Phi(v) \, \frac{F}{m_{\mathrm{e}}} \cdot \nabla_v f \, dv = \int \Phi(v) \left(\frac{\partial f}{\partial t} \right)_{\mathrm{coll}} dv \tag{6}$$

By invoking the definition of the average quantity (5), the first term on the left-hand side (LHS) of (6) can be rewritten as

$$\int \Phi \, \frac{\partial f}{\partial t} \, dv = \frac{\partial}{\partial t} \int \Phi f \, dv = \frac{\partial}{\partial t} [n \langle \Phi(v) \rangle] \tag{7}$$

Using the integration by parts, the second term of (6) is expressed as

$$\int \Phi \, v \cdot \nabla f \, dv = \int [\nabla \cdot (\Phi v f) - f \, \nabla \cdot (\Phi v)] \, dv \tag{8}$$

Since Φv is not a function of r, $\nabla \cdot (\Phi v) = 0$. The second term becomes

$$\int \Phi \, v \cdot \nabla f \, dv = \int \nabla \cdot (\Phi v f) \, dv = \nabla \cdot \int \Phi v f \, dv = \nabla \cdot [n \langle \Phi(r) v \rangle] \tag{9}$$

Applying integration by parts and the Gauss divergence theorem, the third term of (6) can be rewritten as

3

$$\int \Phi(\boldsymbol{v}) \frac{\boldsymbol{F}}{m_{\mathrm{e}}} \cdot \nabla_{\boldsymbol{v}} f \, \mathrm{d}\boldsymbol{v} = \int \left[\nabla_{\boldsymbol{v}} \cdot \left(\Phi \frac{\boldsymbol{F}}{m_{\mathrm{e}}} f \right) - f \, \nabla_{\boldsymbol{v}} \cdot \left(\Phi \frac{\boldsymbol{F}}{m_{\mathrm{e}}} \right) \right] \mathrm{d}\boldsymbol{v}$$
$$= \frac{1}{m_{\mathrm{e}}} \oint \Phi \frac{\boldsymbol{F}}{m_{\mathrm{e}}} f \, \mathrm{d}\boldsymbol{S}_{\boldsymbol{v}} - \frac{1}{m_{\mathrm{e}}} \int \nabla_{\boldsymbol{v}} \cdot (\Phi \boldsymbol{F}) \, f \, \mathrm{d}\boldsymbol{v} \tag{10}$$

where $\boldsymbol{S}_{\boldsymbol{v}}$ is the boundary of the velocity space at infinity. Since no particle travels at an infinite speed, $f = 0$ at $v \to \infty$ and the contour integral in (10) vanishes. As a result, (10) becomes

$$\int \Phi \frac{\boldsymbol{F}}{m_{\mathrm{e}}} \cdot \nabla_{\boldsymbol{v}} f \, \mathrm{d}\boldsymbol{v} = -\frac{1}{m_{\mathrm{e}}} \int \nabla_{\boldsymbol{v}} \cdot (\Phi \boldsymbol{F}) \, f \, \mathrm{d}\boldsymbol{v} = -\frac{n}{m_{\mathrm{e}}} \langle \nabla_{\boldsymbol{v}} \cdot (\Phi \boldsymbol{F}) \rangle$$
$$= -\frac{n}{m_{\mathrm{e}}} \langle \nabla_{\boldsymbol{v}} \Phi \cdot \boldsymbol{F} \rangle - \frac{n}{m_{\mathrm{e}}} \langle \Phi \, \nabla_{\boldsymbol{v}} \cdot \boldsymbol{F} \rangle \tag{11}$$
$$= -\frac{n}{m_{\mathrm{e}}} \langle \nabla_{\boldsymbol{v}} \Phi \cdot \boldsymbol{F} \rangle$$

In reaching (11), $\nabla_{\boldsymbol{v}} \cdot \boldsymbol{F} = 0$ is applied since the Lorentz force is divergence-free in the velocity space.

The RHS of (6) is denoted as

$$\int \Phi(\boldsymbol{v}) \left(\frac{\partial f}{\partial t} \right)_{\mathrm{coll}} \mathrm{d}\boldsymbol{v} = \left(\frac{\partial n \langle \Phi(\boldsymbol{v}) \rangle}{\partial t} \right)_{\mathrm{coll}} \tag{12}$$

at this moment, and will be discussed in the following sections.

Finally, the general transport equation can be expressed as

$$\frac{\partial n \langle \Phi \rangle}{\partial t} + \nabla \cdot (n \langle \Phi \boldsymbol{v} \rangle) - \frac{n}{m_{\mathrm{e}}} \langle \boldsymbol{F} \cdot \nabla_{\boldsymbol{v}} \Phi \rangle = \left(\frac{\partial n \langle \Phi \rangle}{\partial t} \right)_{\mathrm{coll}} \tag{13}$$

which is the conservation equation for the density of the macroscopically averaged quantity $\langle \Phi \rangle$.

3.1.2 Five-Moment Plasma Fluid Model

Plasma fluid models can be obtained by taking moments of the Boltzmann equation. In this section, the five-moment fluid model is derived by taking the first three moments. Higher-order fluid models, such as the ten-moment and the 13-moment models, can also be obtained in the same manner.

3.1.2.1 The Particle Continuity Equation

In (13), setting $\Phi = 1$ yields the particle continuity equation

$$\frac{\partial n}{\partial t} + \nabla \cdot (n \boldsymbol{U}) = \left(\frac{\partial n}{\partial t} \right)_{\mathrm{coll}} = (v_{\mathrm{i}} - v_{\mathrm{a}}) n \tag{14}$$

4

where ν_i and ν_a stand for the ionization and attachment frequencies in the ionization and attachment collision processes, respectively, which can be physically interpreted as the number of particles created and annihilated per unit time per unit volume due to collisions.

3.1.2.2   The Momentum Conservation Equation

Taking $\Phi = m_e \boldsymbol{v}$ yields the momentum conservation equation. In (13), $\langle \Phi \rangle = m_e \langle \boldsymbol{v} \rangle = m_e \boldsymbol{U}$ and $\langle \Phi \boldsymbol{v} \rangle = m_e \langle \boldsymbol{v}\boldsymbol{v} \rangle$. Let $\boldsymbol{v} = \boldsymbol{U} + \boldsymbol{q}$, where $\boldsymbol{q}$ stands for the velocity fluctuation around the mean value $\boldsymbol{U}$, we have

$$\langle \Phi \boldsymbol{v} \rangle = m_e \langle \boldsymbol{v}\boldsymbol{v} \rangle = m_e(\langle \boldsymbol{U}\boldsymbol{U} \rangle + \langle \boldsymbol{U}\boldsymbol{q} \rangle + \langle \boldsymbol{q}\boldsymbol{U} \rangle + \langle \boldsymbol{q}\boldsymbol{q} \rangle) = m_e(\boldsymbol{U}\boldsymbol{U} + \langle \boldsymbol{q}\boldsymbol{q} \rangle) \tag{15}$$

Defining the (symmetric) pressure tensor

$$\mathbb{P} = m_e \int \boldsymbol{q}\boldsymbol{q} \, f \, \mathrm{d}\boldsymbol{v} = m_e \int (\boldsymbol{v} - \boldsymbol{U})(\boldsymbol{v} - \boldsymbol{U}) \, f \, \mathrm{d}\boldsymbol{v} = m_e n \langle \boldsymbol{q}\boldsymbol{q} \rangle \tag{16}$$

yields

$$\langle \Phi \boldsymbol{v} \rangle = m_e \boldsymbol{U}\boldsymbol{U} + \frac{1}{n}\mathbb{P} \tag{17}$$

The second term of (13) can be expressed as

$$\nabla \cdot (n\langle \Phi \boldsymbol{v} \rangle) = \nabla \cdot (m_e n \boldsymbol{U}\boldsymbol{U} + \mathbb{P}) = m_e \nabla \cdot \left(n\boldsymbol{U}\boldsymbol{U} + \frac{1}{m_e}\mathbb{P} \right) \tag{18}$$

In the third term of (13), $\nabla_{\boldsymbol{v}}\Phi = m_e \nabla_{\boldsymbol{v}}\boldsymbol{v} = m_e \mathbb{I}$, where $\mathbb{I}$ is an identity tensor. Therefore, the third term becomes

$$-\frac{n}{m_e}\langle \boldsymbol{F} \cdot \nabla_{\boldsymbol{v}}\Phi \rangle = -\frac{n}{m_e}\langle \boldsymbol{F} \cdot m_e\mathbb{I} \rangle = -n\langle q_e(\boldsymbol{E} + \boldsymbol{v}\times\boldsymbol{B}) \rangle = -q_e(n\boldsymbol{E} + n\boldsymbol{U}\times\boldsymbol{B}) \tag{19}$$

where q_e denotes the electron charge.

Finally, the momentum conservation equation is obtained as

$$\begin{aligned}
\frac{\partial n\boldsymbol{U}}{\partial t} + \nabla \cdot \left(n\boldsymbol{U}\boldsymbol{U} + \frac{1}{m_e}\mathbb{P} \right) &= \frac{q_e}{m_e}(n\boldsymbol{E} + n\boldsymbol{U}\times\boldsymbol{B}) + \frac{1}{m_e}\left(\frac{\partial n\boldsymbol{U}}{\partial t} \right)_{\mathrm{coll}} \\
&= \frac{q_e}{m_e}(n\boldsymbol{E} + n\boldsymbol{U}\times\boldsymbol{B}) - \nu_c n\boldsymbol{U}
\end{aligned} \tag{20}$$

where ν_c stands for the total collision frequency.

5

3.1.2.3 The Energy Conservation Equation

The energy conservation equation can be obtained by taking $\Phi = \frac{1}{2}m_e v^2$. In the first term of (13), $\langle \Phi \rangle = \frac{1}{2}m_e \langle v^2 \rangle = \mathcal{E}$ and in the second term, $n\langle \Phi v \rangle = \frac{1}{2}m_e n \langle v^2 v \rangle = \mathcal{E}$. Using the definition of the average quantity (5), we have

$$
\begin{aligned}
n\langle v^2 v \rangle &= \int v^2 v\, f\, \mathrm{d}v = \int (q + U)\cdot(q + U)(q + U)\, f\, \mathrm{d}v \\
&= \int q^2 q\, f\, \mathrm{d}v + 2U \cdot \int qq\, f\, \mathrm{d}v + \frac{2n}{m_e}\mathcal{E}U \\
&= \frac{2}{m_e}(Q + \mathbb{P}\cdot U + nU\mathcal{E})
\end{aligned}
\tag{21}
$$

In deriving the above expression, the definition of the pressure tensor (16) has been employed, and the heat flux vector is defined as

$$
Q = \frac{m_e}{2}\int q^2 q\, f\, \mathrm{d}v = \frac{m_e}{2}\int |v - U|^2 (v - U)\, f\, \mathrm{d}v
\tag{22}
$$

As a result, the second term in the general transport equation becomes

$$
\nabla \cdot (n\langle \Phi v \rangle) = \nabla \cdot (nU\mathcal{E} + \mathbb{P}\cdot U + Q)
\tag{23}
$$

The third term in the general transport equation can be written as

$$
\begin{aligned}
-\frac{n}{m_e}\langle F \cdot \nabla_v \Phi \rangle &= -\frac{n}{m_e}\frac{1}{n}\int F \cdot \nabla_v \left(\frac{1}{2}m_e v^2\right) f\, \mathrm{d}v = -\int F \cdot v\, f\, \mathrm{d}v \\
&= -\int q_e(E + v\times B)\cdot v\, f\, \mathrm{d}v = -\int q_e E \cdot v\, f\, \mathrm{d}v \\
&= -q_e E \cdot nU
\end{aligned}
\tag{24}
$$

Finally, the energy conservation equation can be expressed as

$$
\frac{\partial n\mathcal{E}}{\partial t} + \nabla \cdot (nU\mathcal{E} + \mathbb{P}\cdot U + Q) = q_e E \cdot nU + \left(\frac{\partial n\mathcal{E}}{\partial t}\right)_{\mathrm{coll}} = q_e E \cdot nU - Q_e n
\tag{25}
$$

where Q_e stands for the electron energy loss frequency.

Equations (14), (20), and (25) are the governing equations of the five-moment plasma fluid model. The name "five-moment" refers to the five scalar quantities governed by the model, which are n, U_x, U_y, U_z, and $\mathcal{E}$.

It should be noted that the equations obtained from the general transport equation are not closed. Due to the second term $\nabla \cdot (n\langle \Phi v \rangle)$, the n-th moment equation will always introduce the $(n + 1)$-

6

th macroscopic moment. As a result, any finite set of moment equations have more unknowns than equations. To obtain a closed model, some additional information, limiting assumption, or additional physical setting, is always needed.

In the five-moment model, the higher-order moment, the heat flux vector $\boldsymbol{Q}$, is ignored, and the pressure tensor is assumed to be diagonal and isotropic $\mathbb{P} = P\mathbb{I}$, where P is the scalar pressure defined as

$$P = \frac{1}{3}\mathrm{tr}(\mathbb{P}) = \frac{m_e}{3}\int \mathrm{tr}[(\boldsymbol{v} - \boldsymbol{U})(\boldsymbol{v} - \boldsymbol{U})]\, f\, \mathrm{d}\boldsymbol{v} = \frac{m_e}{3}\int |\boldsymbol{v} - \boldsymbol{U}|^2 f\, \mathrm{d}\boldsymbol{v} \tag{26}$$

in three dimensions. In a N-dimensional problem, the factor $1/3$ becomes $1/N$. In the above expression, tr stands for the matrix trace. From the ideal gas law, the pressure and the temperature are related by the equation of state $P = n\,k_B T$, where $k_B = 8.617 \times 10^{-5}$ eV/K is the Boltzmann constant and T is the temperature in Kelvin. From (26), it can be seen that

$$\begin{aligned}\frac{P}{n} &= k_B T = \frac{1}{n}\frac{m_e}{3}\int |\boldsymbol{v} - \boldsymbol{U}|^2 f\, \mathrm{d}\boldsymbol{v} = \frac{1}{n}\frac{m_e}{3}\int (v^2 + U^2 - \boldsymbol{v}\cdot\boldsymbol{U} - \boldsymbol{U}\cdot\boldsymbol{v})\, f\, \mathrm{d}\boldsymbol{v} \\ &= \frac{2}{3}\left(\mathcal{E} - \frac{1}{2}m_e U^2\right)\end{aligned} \tag{27}$$

Therefore, the pressure and the energy are related by

$$n\mathcal{E} = \frac{3}{2}P + \frac{1}{2}m_e n U^2 \tag{28}$$

Apparently, $n\mathcal{E}$ stands for the total energy for n particles, $\frac{3}{2}P$ and $\frac{1}{2}m_e n U^2$ stand for the total internal and kinetic energy for n particles, respectively. In general,

$$n\mathcal{E} = \frac{P}{\gamma - 1} + \frac{1}{2}m_e n U^2 \tag{29}$$

where $\gamma = (N + 2)/N$ is the ratio of specific heats, which equals to 5/3 for electrons in three dimensions and 1.4 for air particles.

With the heat flux ignored and the scalar closure between the pressure and the energy assumed, the five-moment plasma fluid model is finally presented as

$$\frac{\partial n}{\partial t} + \nabla \cdot (n\boldsymbol{U}) = (v_i - v_a)n \tag{30}$$

$$\frac{\partial n\boldsymbol{U}}{\partial t} + \nabla \cdot \left(n\boldsymbol{U}\boldsymbol{U} + \frac{1}{m_e}P\mathbb{I}\right) = \frac{q_e}{m_e}(n\boldsymbol{E} + n\boldsymbol{U}\times\boldsymbol{B}) - v_c n\boldsymbol{U} \tag{31}$$

$$\frac{\partial n\mathcal{E}}{\partial t} + \nabla \cdot [\boldsymbol{U}(n\mathcal{E} + P)] = q_e \boldsymbol{E} \cdot n\boldsymbol{U} - Q_e n \tag{32}$$

7

3.1.3 Collision Reactions, Transport Coefficients, & Electron Energy Distribution Function

When electrons are pushed to move by the Lorentz force, they collide with neutral air particles frequently. Depending on the energy that different electrons possess, collision events may trigger different reactions. Generally, there are two major types of collisions, namely, elastic and inelastic collisions. In an elastic collision event, the electron collides with a neutral air particle (a nitrogen or an oxygen molecule, for example), gets bounced to some scattering angle depending on the angle of incidence and losses a part of its momentum and energy. For an inelastic collision, there are several possibilities. First, the electron may get attached to (absorbed by) the air particle and result in a negative ion, which is called an attachment reaction. Second, if the electron has a higher energy, it can excite the air particle, making the air particle rotate, vibrate, or get excited to a higher energy level. Such a collision process is called an excitation reaction. Third, if the electron has an even higher energy, it is able to kick out a new electron from the air particle, which is known as an ionization reaction. In this work, air is simply treated as 20% oxygen plus 80% nitrogen. Various collision reactions between the electron and the oxygen and nitrogen molecules are summarized in Table 1 and Table 2, respectively. In these two tables, ε_k stands for the threshold (minimum) energy for the k-th collision reaction to take place.

Table 1. Electron–Oxygen Collision Reactions [31], [32]

Index	Collision Type	Reaction Formula	ε_k (eV)
O1	Three-body attachment	$e + O_2 \longrightarrow O_2^{-*};\ O_2^{-*} + O_2 \longrightarrow O_2^- + O_2$	0
O2	Two-body attachment	$e + O_2 \longrightarrow O^- + O$	0
O3	Effective momentum transfer	$e + O_2 \longrightarrow e + O_2$	0
O4	Rotational excitation	$e + O_2 \longrightarrow e + O_2(\text{rot})$	0.02
O5	Vibrational excitation	$e + O_2 \longrightarrow e + O_2(v = 1)$	0.19
O6	Vibrational excitation	$e + O_2 \longrightarrow e + O_2(v = 1\text{res})$	0.19
O7	Vibrational excitation	$e + O_2 \longrightarrow e + O_2(v = 2)$	0.38
O8	Vibrational excitation	$e + O_2 \longrightarrow e + O_2(v = 2\text{res})$	0.38
O9	Vibrational excitation	$e + O_2 \longrightarrow e + O_2(v = 3)$	0.57
O10	Vibrational excitation	$e + O_2 \longrightarrow e + O_2(v = 4)$	0.75
O11	Metastable excitation	$e + O_2 \longrightarrow e + O_2(a^1\Delta_g)$	0.977
O12	Metastable excitation	$e + O_2 \longrightarrow e + O_2(b^1\Sigma_g^+)$	1.627
O13	Metastable excitation	$e + O_2 \longrightarrow e + O_2(c^1\Sigma_u^- A^+\Sigma_u^+)$	4.5
O14	Dissociative excitation	$e + O_2 \longrightarrow e + O(3P) + O(3P)$	6.0
O15	Dissociative excitation	$e + O_2 \longrightarrow e + O(3P) + O(1D)$	8.4
O16	Dissociative excitation	$e + O_2 \longrightarrow e + O(1D) + O(1D)$	9.97
O17	Ionization	$e + O_2 \longrightarrow 2e + O_2^+$	12.06

8

Table 2. Electron–Nitrogen Collision Reactions [33], [34]

Index	Collision Type	Reaction Formula	ε_k (eV)
N1	Elastic momentum transfer	$e + N_2 \longrightarrow e + N_2$	0
N2	Rotational excitation	$e + N_2 \longrightarrow e + N_2(\text{rot})$	0.02
N3	Vibrational excitation	$e + N_2 \longrightarrow e + N_2(v = 1\text{res})$	0.29
N4	Vibrational excitation	$e + N_2 \longrightarrow e + N_2(v = 1)$	0.291
N5	Vibrational excitation	$e + N_2 \longrightarrow e + N_2(v = 2)$	0.59
N6	Vibrational excitation	$e + N_2 \longrightarrow e + N_2(v = 3)$	0.88
N7	Vibrational excitation	$e + N_2 \longrightarrow e + N_2(v = 4)$	1.17
N8	Vibrational excitation	$e + N_2 \longrightarrow e + N_2(v = 5)$	1.47
N9	Vibrational excitation	$e + N_2 \longrightarrow e + N_2(v = 6)$	1.76
N10	Vibrational excitation	$e + N_2 \longrightarrow e + N_2(v = 7)$	2.06
N11	Vibrational excitation	$e + N_2 \longrightarrow e + N_2(v = 8)$	2.35
N12	Electronic excitation	$e + N_2 \longrightarrow e + N_2(A3, v = 0 - 4)$	6.17
N13	Electronic excitation	$e + N_2 \longrightarrow e + N_2(A3, v = 5 - 9)$	7.00
N14	Electronic excitation	$e + N_2 \longrightarrow e + N_2(B3)$	7.35
N15	Electronic excitation	$e + N_2 \longrightarrow e + N_2(W3)$	7.36
N16	Electronic excitation	$e + N_2 \longrightarrow e + N_2(A3, v \geq 10)$	7.80
N17	Electronic excitation	$e + N_2 \longrightarrow e + N_2(B'3)$	8.16
N18	Electronic excitation	$e + N_2 \longrightarrow e + N_2(a'1)$	8.40
N19	Electronic excitation	$e + N_2 \longrightarrow e + N_2(a1)$	8.55
N20	Electronic excitation	$e + N_2 \longrightarrow e + N_2(w1)$	8.89
N21	Electronic excitation	$e + N_2 \longrightarrow e + N_2(C3)$	11.03
N22	Electronic excitation	$e + N_2 \longrightarrow e + N_2(E3)$	11.87
N23	Electronic excitation	$e + N_2 \longrightarrow e + N_2(a''1)$	12.25
N24	Electronic excitation	$e + N_2 \longrightarrow e + N_2(\text{sum of singlet states})$	13.0
N25	Ionization	$e + N_2 \longrightarrow 2e + N_2^+$	15.6

The various collision reactions result in the generation and annihilation of electrons and the momentum and energy change of electrons, which are accounted for by the transport coefficients, including the total ionization coefficient ν_i, the total attachment coefficient ν_a, the total collision frequency ν_c, and the energy loss frequency Q_e. These transport coefficients are critical parameters that determine the behavior of the breakdown process and are defined as the integration of the corresponding collision cross sections multiplied by the EEDF, over the entire energy spectrum as follows [15]:

9

$$v_i = N_{\text{Air}} \sqrt{\frac{2}{m_e}} \int_{\varepsilon_k}^{\infty} \left(\sum_{k=\text{ionization}} x_k \sigma_k \right) \varepsilon F_0 d\varepsilon \tag{33}$$

$$v_a = N_{\text{Air}} \sqrt{\frac{2}{m_e}} \int_{\varepsilon_k}^{\infty} \left(\sum_{k=\text{attachment}} x_k \sigma_k \right) \varepsilon F_0 d\varepsilon \tag{34}$$

$$v_c = N_{\text{Air}} \sqrt{\frac{2}{m_e}} \int_{\varepsilon_k}^{\infty} \left(\sum_{k=\text{all}} x_k \sigma_k \right) \varepsilon F_0 d\varepsilon \tag{35}$$

$$Q_e = N_{\text{Air}} \sqrt{\frac{2}{m_e}} \sum_{k=\text{elastic}} \frac{2m_e}{M_k} \int_{\varepsilon_k}^{\infty} x_k \left[\sigma_k \left(\varepsilon^2 F_0 + \frac{k_B T}{q_e} \frac{dF_0}{d\varepsilon} \right) \right] d\varepsilon$$

$$+ N_{\text{Air}} \sqrt{\frac{2}{m_e}} \sum_{k=\text{inelastic}} \varepsilon_k \int_{\varepsilon_k}^{\infty} x_k \sigma_k \varepsilon F_0 d\varepsilon \tag{36}$$

where N_{Air} denotes the number density of the ambient air, x_k and M_k denote the mole fraction and the mass of the target gas species of collision process k, respectively, σ_k denotes the cross section of collision process k, and F_0 denotes the EEDF normalized by

$$\int_0^{\infty} \varepsilon^{\frac{1}{2}} F_0(\varepsilon) d\varepsilon = 1 \tag{37}$$

which has units of $eV^{-\frac{3}{2}}$.

In the above definitions, the collision cross sections are obtained from either analytical calculations or experimental measurements and are usually tabulated as functions of electron energy. The EEDF is usually solved from the Boltzmann equation. For an equilibrium process, the EEDF has a Maxwellian distribution which, when normalized by (37), becomes a straight line in a logarithmic plot, with the slope being $-1/k_B T$. The high-power breakdown process, however, is highly non-equilibrium. As a result, the Maxwellian distribution is not appropriate in describing the electron energy distribution in such a process. To obtain a proper distribution function, the classic two-term approximation can be used to solve the Boltzmann equation taking into consideration the breakdown process, where the electron distribution function f is expanded in terms of spherical harmonics as [15]

$$f(\boldsymbol{r}, \boldsymbol{v}, t) = \frac{1}{2\pi} \left(\frac{m_e}{2} \right)^{\frac{3}{2}} n(\boldsymbol{r}, t)[F_0(\varepsilon) + F_1(\varepsilon) \cos \theta] \tag{38}$$

where F_0 is the EEDF representing the isotropic part of the electron distribution f and F_1 is the anisotropic perturbation of f. Once the proper EEDF is obtained, it can be used to integrate with the corresponding cross sections to calculate the transport coefficients, which are then used in the five-moment model to calculate the macroscopic fluid parameters.

10

3.2 Coupled Electromagnetics--Plasma System

The high-power air breakdown process can be described by the following coupled electromagnetic--plasma system

$$\epsilon\frac{\partial \boldsymbol{E}}{\partial t} - \nabla\times\boldsymbol{H} = -q_e n\boldsymbol{U} \tag{39}$$

$$\mu\frac{\partial \boldsymbol{H}}{\partial t} + \nabla\times\boldsymbol{E} = 0 \tag{40}$$

$$\frac{\partial n}{\partial t} + \nabla\cdot(n\boldsymbol{U}) = (\nu_i - \nu_a)n \tag{41}$$

$$\frac{\partial n\boldsymbol{U}}{\partial t} + \nabla\cdot\left(n\boldsymbol{U}\boldsymbol{U} + \frac{1}{m_e}P\mathbb{I}\right) = \frac{q_e}{m_e}(n\boldsymbol{E} + n\boldsymbol{U}\times\boldsymbol{B}) - \nu_c n\boldsymbol{U} \tag{42}$$

$$\frac{\partial n\mathcal{E}}{\partial t} + \nabla\cdot[\boldsymbol{U}(n\mathcal{E} + P)] = q_e\boldsymbol{E}\cdot n\boldsymbol{U} - Q_e n \tag{43}$$

In the above equations, ϵ and μ denote the permittivity and permeability of the medium, respectively. The electric and magnetic fields $\boldsymbol{E}$ and $\boldsymbol{H}$ are governed by Maxwell's equations (39) and (40), while the electron density n, mean velocity $\boldsymbol{U}$, mean energy $\mathcal{E}$ and pressure P are governed by the five-moment plasma fluid equations (41)--(43), which are essentially the compressible Euler equations in fluid dynamics. As described in the preceding section, in order to close the system, the heat flux is neglected and the scalar closure is applied to relate the energy and the pressure as $n\mathcal{E} = \frac{P}{\gamma-1} + \frac{1}{2}m_e nU^2$.

3.3 The DGTD Solution of the Coupled System

To solve the coupled equations using the DGTD method, both Maxwell's and the Euler equations are first written uniformly into the following conservation form

$$\mathfrak{D}\frac{\partial \boldsymbol{G}}{\partial t} + \nabla\cdot\mathfrak{F}(\boldsymbol{G}) = \boldsymbol{S}(\boldsymbol{G}) \tag{44}$$

where $\mathfrak{D}$ denotes the material parameter tensor, $\boldsymbol{G}$ denotes the unknown quantity vector which consists of the conservative variables, $\mathfrak{F}$ denotes the physical flux tensor and $\boldsymbol{S}$ denotes the source term.

The strong form of these governing equations can then be expressed as

$$\int_{V_e} l_i \mathfrak{D}\frac{\partial \boldsymbol{G}}{\partial t}\,dV = -\int_{V_e} l_i \nabla\cdot\mathfrak{F}(\boldsymbol{G})\,dV - \oint_{\partial V_e} l_i(\mathfrak{F}^* - \mathfrak{F})\cdot\hat{\boldsymbol{n}}\,dS + \int_{V_e} l_i \boldsymbol{S}(\boldsymbol{G})\,dV \tag{45}$$

where l_i stands for the testing function defined in the tetrahedral element V_e and $(\mathfrak{F}^* - \mathfrak{F})\cdot\boldsymbol{n}\hat{}$ refers to the total flux defined on the boundary of each tetrahedral element.

11

3.3.1 Maxwell's Equations

For Maxwell's equations, the material parameter tensor is

$$\mathfrak{D} = \text{diag}\{\epsilon, \epsilon, \epsilon, \mu, \mu, \mu\} \tag{46}$$

the conservative variables are simply chosen as (with T being the transpose operator)

$$\boldsymbol{G} = (E_1, E_2, E_3, H_1, H_2, H_3)^{\text{T}} \tag{47}$$

the flux tensor is

$$\mathfrak{F} = \begin{pmatrix} 0 & -H_3 & H_2 \\ H_3 & 0 & -H_1 \\ -H_2 & H_1 & 0 \\ 0 & E_3 & -E_2 \\ -E_3 & 0 & E_1 \\ E_2 & -E_1 & 0 \end{pmatrix} \tag{48}$$

and the source term is

$$\boldsymbol{S} = \left(-q_e n U_x, -q_e n U_y, -q_e n U_z, 0, 0, 0\right)^{\text{T}} \tag{49}$$

Due to their hyperbolic property, the upwind flux can be used for Maxwell's equations [14], [18]

$$(\mathfrak{F}^* - \mathfrak{F}) \cdot \hat{\boldsymbol{n}} = \begin{bmatrix} \dfrac{1}{\langle Y \rangle} (Y^+ \, \hat{\boldsymbol{n}} \times [\![\boldsymbol{E}]\!] + \hat{\boldsymbol{n}} \times \hat{\boldsymbol{n}} \times [\![\boldsymbol{H}]\!]) \\ \dfrac{1}{\langle Z \rangle} (Z^+ \, \hat{\boldsymbol{n}} \times [\![\boldsymbol{H}]\!] - \hat{\boldsymbol{n}} \times \hat{\boldsymbol{n}} \times [\![\boldsymbol{E}]\!]) \end{bmatrix} \tag{50}$$

In the above expression, the addition $\langle \cdot \rangle$ and jump $[\![\cdot]\!]$ functions are defined as follows

$$\langle a \rangle = a^+ + a^-, \qquad [\![a]\!] = a^+ - a^- \tag{51}$$

where the superscripts $-$ and $+$ indicate the inside and the outside of a surface, respectively. Note that these definitions apply to both scalar and vector variables.

3.3.2 Euler's Equations

For Euler's equations, $\mathfrak{D}$ is an identity tensor, the conservative variables are chosen as

$$\boldsymbol{G} = \left(n, n U_x, n U_y, n U_z, n\mathcal{E}\right)^{\text{T}} \tag{52}$$

12

Once these conservative variables are obtained, the primitive variables can be obtained as $U = nU/n$, $\mathcal{E} = n\mathcal{E}/n$, and $P = (\gamma - 1)\left(n\mathcal{E} - \frac{1}{2}m_e nU^2\right)$, which are needed in the calculation of the flux tensor

$$\mathfrak{F} = \begin{pmatrix} nU_x & nU_y & nU_z \\ nU_x^2 + \dfrac{1}{m_e}P & nU_xU_y & nU_xU_z \\ nU_xU_y & nU_y^2 + \dfrac{1}{m_e}P & nU_yU_z \\ nU_xU_z & nU_yU_z & nU_z^2 + \dfrac{1}{m_e}P \\ U_x(n\mathcal{E} + P) & U_y(n\mathcal{E} + P) & U_z(n\mathcal{E} + P) \end{pmatrix} \tag{53}$$

and the source term

$$S = \begin{pmatrix} [v_i(\mathcal{E}) - v_a(\mathcal{E})]n \\ \dfrac{q_e}{m_e}[n(E + E^{inc}) + nU \times (B + B^{inc})] - v_c(\mathcal{E})nU \\ q_e(E + E^{inc}) \cdot nU - Q_e(\mathcal{E})n \end{pmatrix} \tag{54}$$

Here, E^{inc} and B^{inc} stand for the electric field and magnetic flux of the incident high-power pulse, respectively. The transport coefficients are all functions of the mean energy $\mathcal{E}$ and can be obtained by interpolating the tabulated values calculated using the method introduced in the preceding section.

To solve the strong form (45) of the Euler equations, the local Lax-Friedrichs flux [18]

$$(\mathfrak{F}^* - \mathfrak{F}) \cdot \hat{n} = \frac{1}{2}\{[\![\mathfrak{F}]\!] \cdot \hat{n} - \lambda[\![G]\!]\} \tag{55}$$

can be used, where

$$\lambda = \max_{g \in \{G^+, G^-\}} \left\{ |U(g)| + \sqrt{\gamma \frac{P(g)}{m_e n(g)}} \right\} \tag{56}$$

is the characteristic velocity of Euler's equations. The resulting ordinary differential equations from both Maxwell's and Euler's equations are integrated in time using the Runge-Kutta method to obtain the time-domain responses and the coupling between these two physics is carried out through the source terms (49) and (54).

4.0 RESULTS AND DISCUSSION

In this section, several examples are given to illustrate the EEDF and transport coefficients and to demonstrate the breakdown process and behaviors under different conditions. In all the numerical examples, the gas under consideration is ambient air, which is assumed to consist of 80% nitrogen and 20% oxygen, with in total 42 different (elastic and inelastic) collision processes listed in Table 1 and Table 2.

4.1   EEDF & Transport Coefficients

First, the Maxwellian and non-Maxwellian EEDFs at different mean energy are shown in this section to demonstrate their distinct difference. As seen in Figure 1, the EEDFs with the Maxwellian distribution are all straight lines in the semi-log plot, indicating that the number of electrons decreases exponentially as the energy increases. The non-Maxwellian EEDFs obtained by solving the Boltzmann equation using the BOLSIG+ package [15] however, decrease much faster as the energy increases, which indicates that fewer electrons have higher energies in a non-equilibrium case. The higher energy tail of the Maxwellian EEDF results in a larger total ionization frequency $\nu_i - \nu_a$ when the mean energy is higher than 1 eV, as shown in Figure 2a. The total collision (Figure 2b) and power loss (Figure 2c) frequencies for the Maxwellian EEDF are also larger than the non-Maxwellian EEDF at lower mean energies.
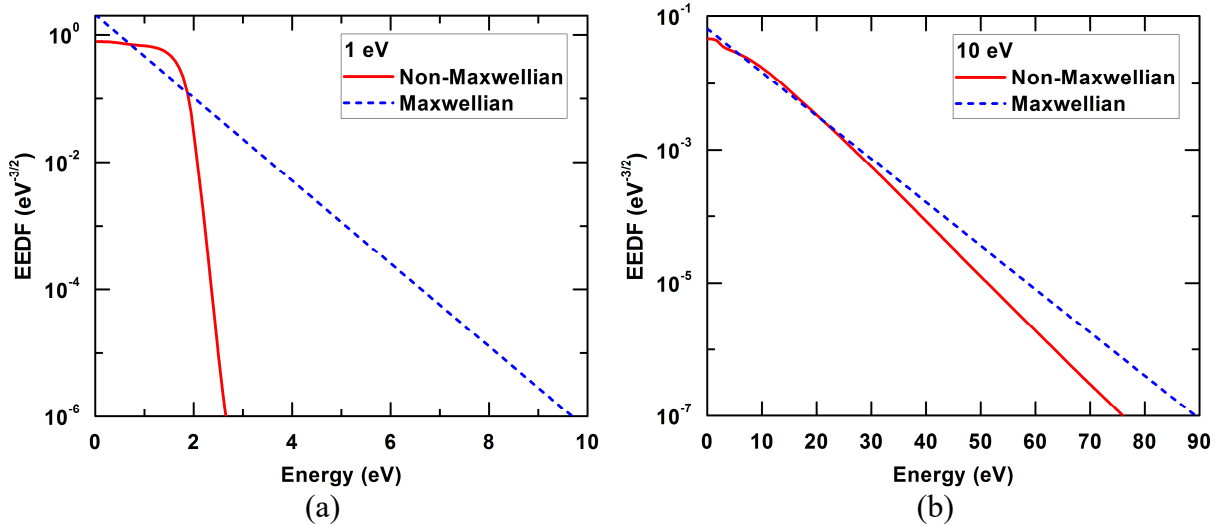

(a)   (b)

Figure 1. The Maxwellian and Non-Maxwellian EEDFs at a Mean Energy of (a) 1 eV and (b) 10 eV
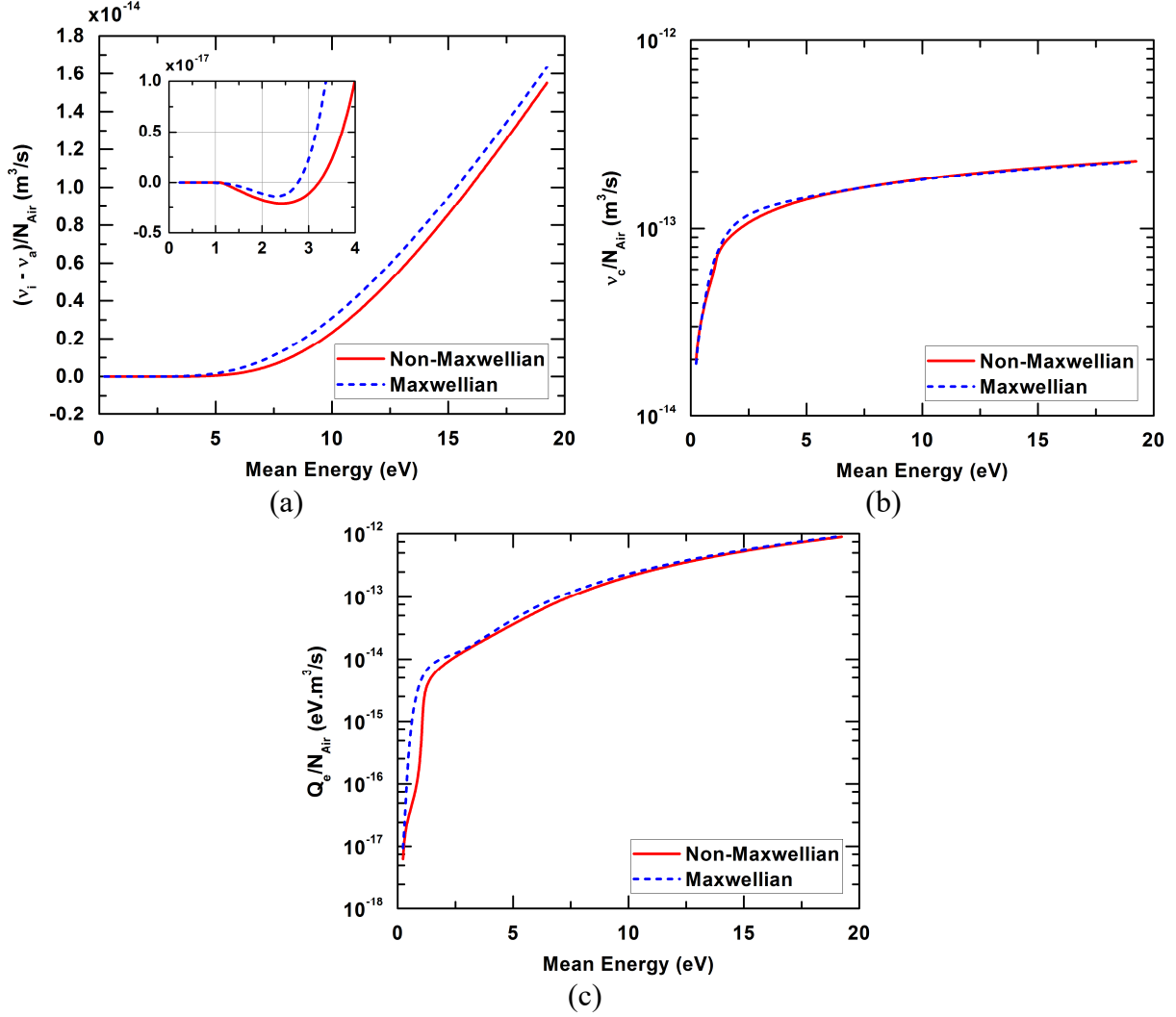
14

Figure 2. The Transport Coefficients as Functions of the Mean Energy, Calculated Using the Maxwellian and Non-Maxwellian EEDFs. (a) Total Ionization Frequency, (b) Total Collision Frequency and (c) Power Loss Frequency

4.2 Air Breakdown Using Different EEDFs

To demonstrate the effects of different EEDFs in the prediction of air breakdown, a numerical example is presented in this section, where a set of 5.5-MV/m, 200-MHz and *y*-polarized modulated difference-of-double-exponentials (DEXP) pulse [37] traveling through air is considered. As illustrated in Figure 3, the simulation domain is 30 m long in the *z*-direction which is truncated with the absorbing boundary condition (ABC) and 0.5 m in both the *x*- and the *y*-directions which are truncated with the perfect electric and magnetic conductors, respectively. The initial electron density in the air is set as $10^6/m^3$. The ambient temperature of the air is set as the room temperature at 300 K and the ambient pressures under consideration is 760 Torr. Figure 4 presents the simulated results using the Maxwellian and non-Maxwellian EEDFs. Clearly, the electric field distribution obtained using the non-Maxwellian EEDF (Figure 4a) remains undisturbed, which is the same as the pulse traveling in the vacuum. However, when the

15

Maxwellian EEDF is used to estimate the transport coefficients, the higher energy tail results in larger ionization coefficient which leads to a larger increase of the electron density, as shown in Figure 4c. The electron density obtained by the Maxwellian EEDF on the plateau is about 100 times larger than that obtained by the non-Maxwellian EEDF. This results in a much larger absorption of the incident field and leads to the tail erosion of the incident HPM pulse, as can be seen in Figure 4a. Other physical parameters, including the electron velocity, energy and temperature, also differ significantly between the results obtained from the Maxwellian and non-Maxwellian distributions. Shown in Figure 4b and Figure 4e are the z-component (the longitudinal component) of the electric field and electron velocity, respectively. This component is present because of the magnetic Lorentz force term $q_e n \boldsymbol{U} \times \boldsymbol{B}$. However, since the U_y component is very small compared to the speed of light, the longitudinal component is very small. But it will become significant when the kinetic energy of the electrons is high enough when compared to the speed of light. Moreover, it is interesting to see that both the electric field E_z and the electron velocity U_z are positive, which is distinctively different from E_y and U_y. This is due to the fact that the U_y and B_x components are always in-phase. Resulted from their cross product, the U_z component becomes purely positive and so does E_z. The positive motion pushes the electrons toward the front edge of the plasma and (partially) results in the large density gradient on the plasma edge. Also, it is very clear that the oscillating frequency of U_z is twice as U_y, due to the higher-order oscillation generated by the magnetic Lorentz force.
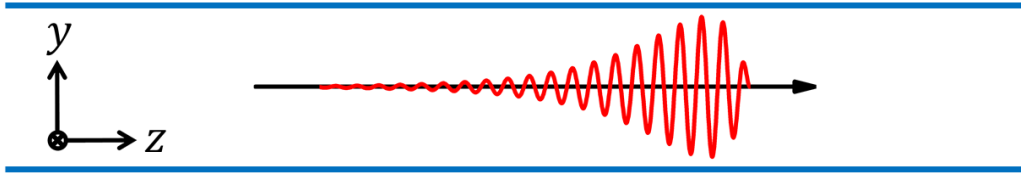

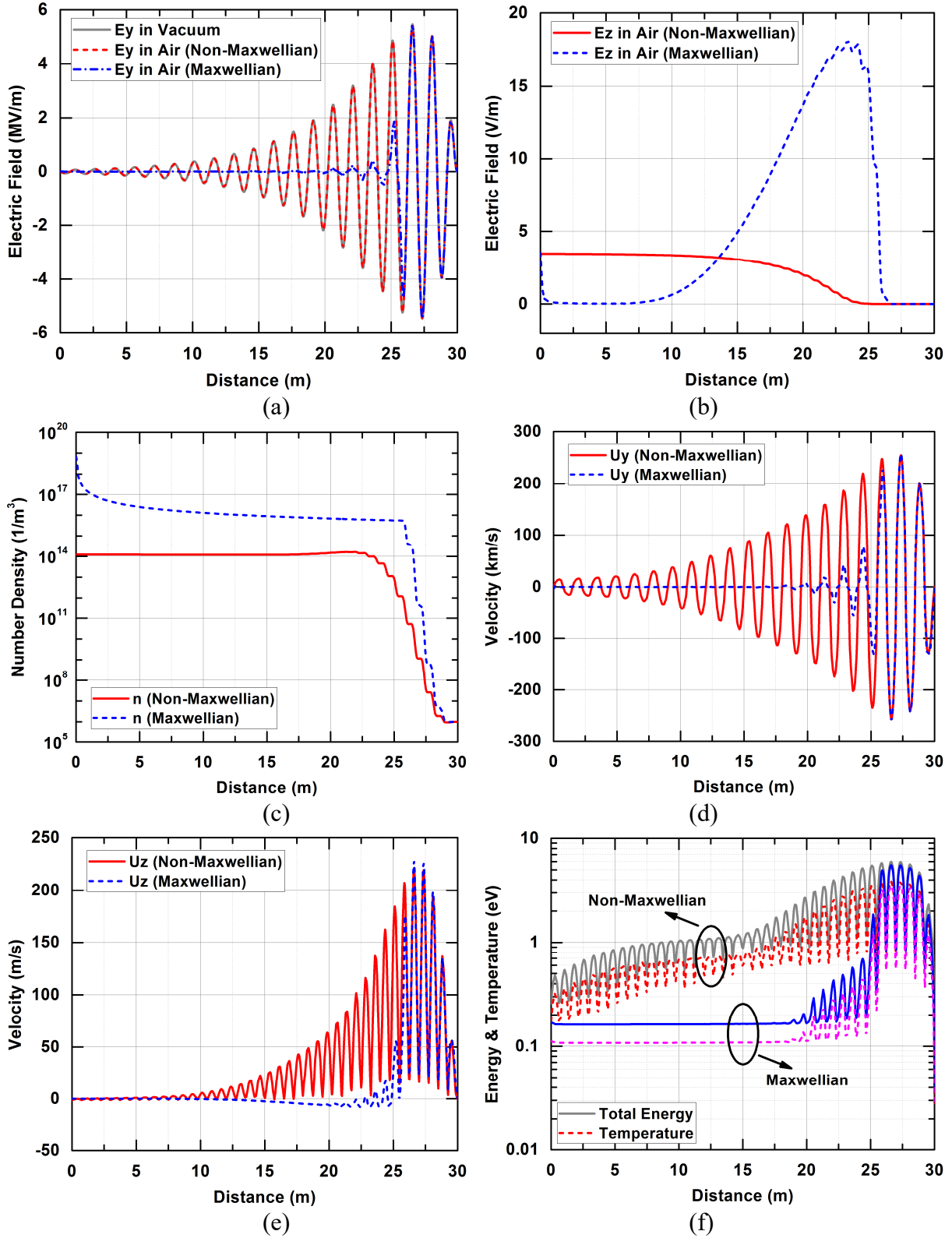**Figure 3. Illustration of the Solution Domain**

Figure 4. The Electric Field, Electron Density, Velocity, Total Energy and Temperature Distributions in Space as the Modulated DEXP Pulse Travels Through the 300-K, 760-Torr Air. Comparisons Are Made Between Using the Maxwellian and Non-Maxwellian EEDFs

17

4.3   Air Breakdown Versus Ambient Pressure

To investigate the breakdown behaviors under different ambient pressures, a set of 300-kV/m, 200-MHz modulated DEXP pulse traveling through air is considered. As in the previous example, the initial electron density in the air is set as $10^6/m^3$ and the ambient temperature of the air is set as the room temperature at 300 K. The ambient pressures under consideration are 600 Torr and 10 Torr, which are referred to as the high- and the low-pressure cases, respectively. Figure 5 and Figure 6 present the simulated results for these two cases, respectively. In the high-pressure case, the air does not break down (see Figure 5c) and the HPM pulse travels through the air undisturbed. This can be seen clearly in Figure 5a where the electric field distribution in the air is the same as that in the vacuum where no breakdown can take place. In the low-pressure case, however, air breakdown takes place and the tail of the HPM pulse cannot travel through the air, as can be seen in Figure 6a and Figure 6c. The effect of pressure on the air breakdown process can be explained as follows. In the high-pressure case, due to the much higher air particle density, the electrons collide much more frequently with air particles, which causes more electron momentum and energy loss. Therefore, it is more difficult for the electron density to increase in the high-pressure case than in the low-pressure case. Compared to the high pressure results shown in Figure 5d and Figure 5f, the electron velocity and energy shown in Figure 6d and Figure 6f are increased to a much higher level, which leads to a much higher ionization frequency that causes the breakdown. This example has been reported in [38].

Figure 5. The Electric Field, Electron Density, Velocity, Total Energy and Temperature Distributions in Space as the Modulated DEXP Pulse Travels Through the 300-K, 600-Torr Air

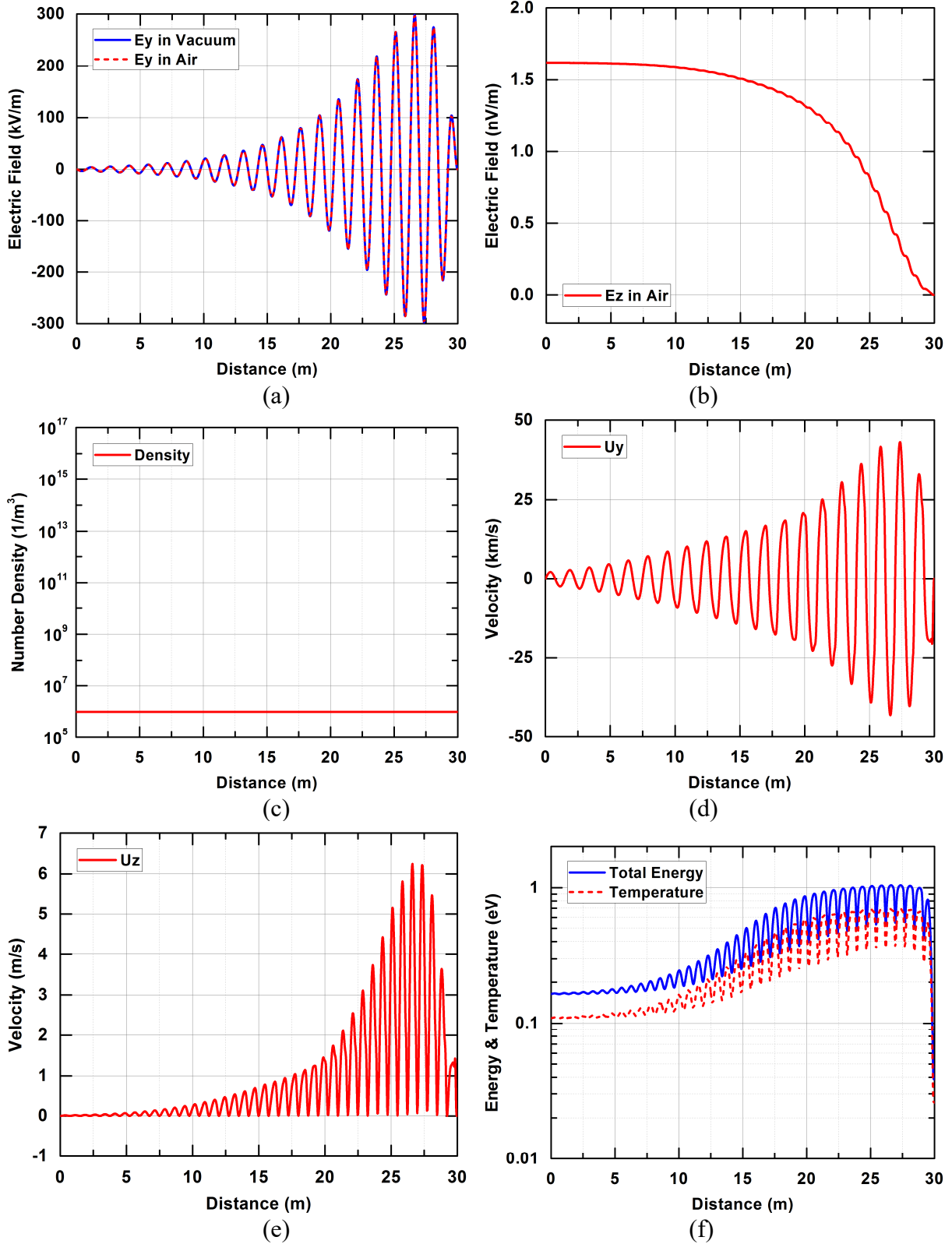19

Figure 6. The Electric Field, Electron Density, Velocity, Total Energy and Temperature Distributions in Space as the Modulated DEXP Pulse Travels Through the 300-K, 10-Torr Air
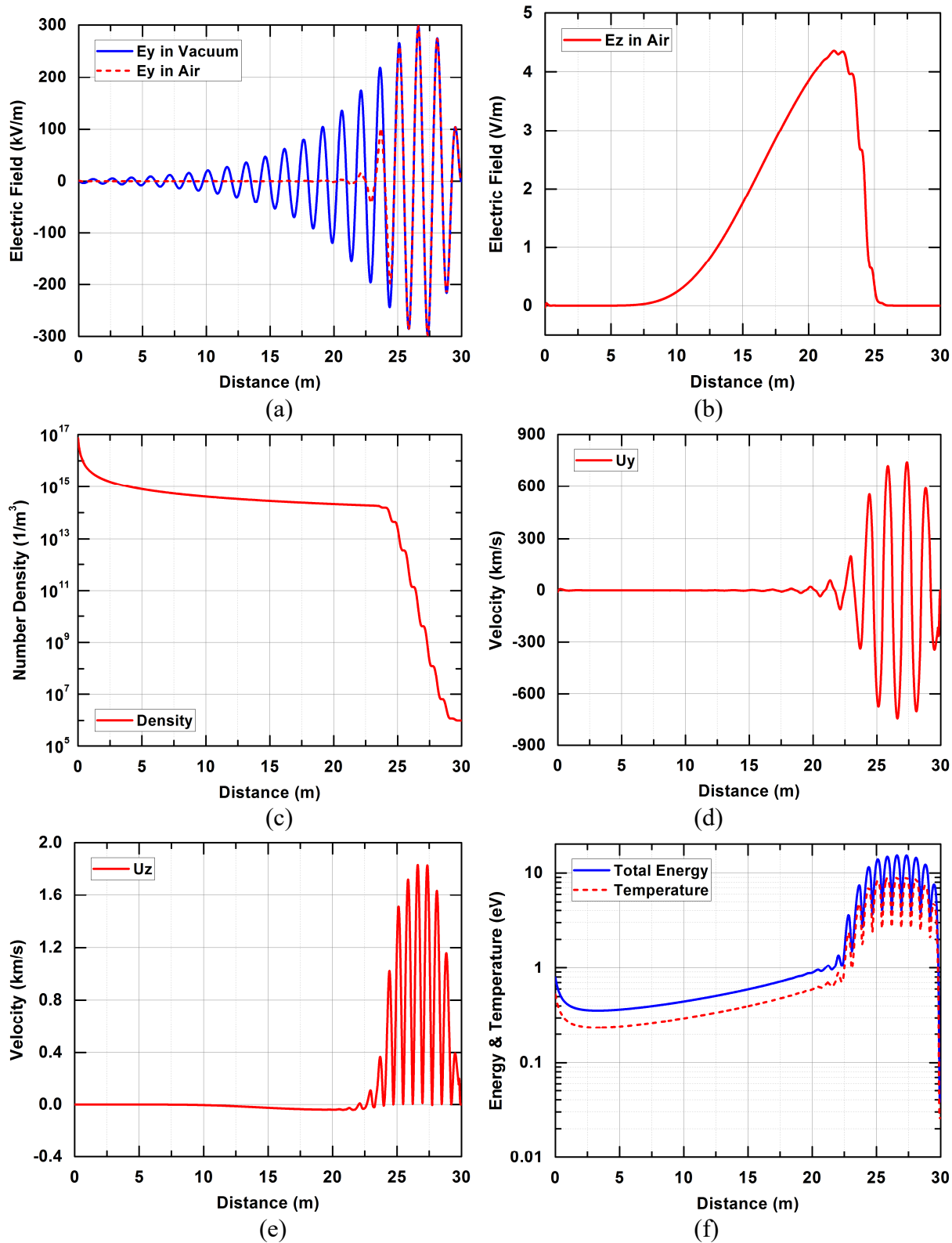
20

Next, the breakdown time as a function of ambient pressure is calculated and presented in Figure 7. The breakdown time is usually defined as the time needed for the electron density to increase to 10^8 times its initial value [39]. In this investigation, a 4.23-MV/m, 2.82-GHz sinusoidal wave travels through air and causes the breakdown. The initial electron density in the air is set as $10^6/m^3$ and the ambient temperature of the air is set as the room temperature at 300 K. In Figure 7, the air breakdown time versus ambient pressure is presented and compared with reference results obtained by a particle-in-cell with Monte-Carlo collision (PIC-MCC) simulation [39], [40] and a fluid simulation with a modified EEDF [9]. Excellent agreement is observed, which validates our implementation of the coupled DGTD solver.
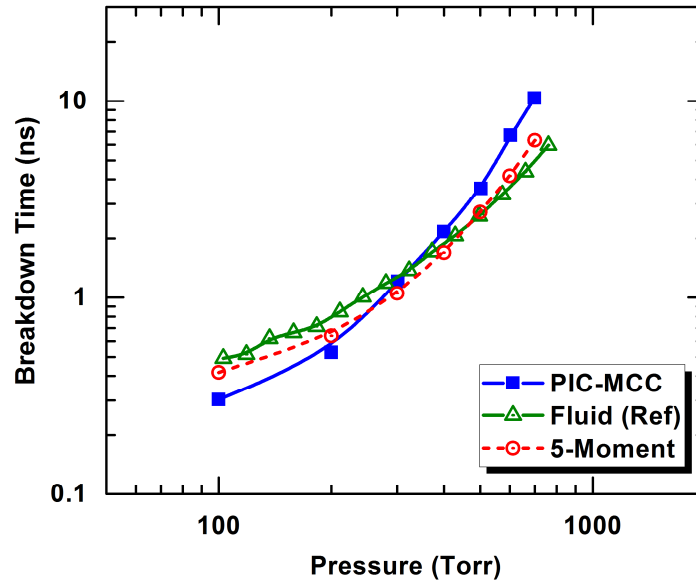

Figure 7. Breakdown Time in Air at 4.23 MV/m and 2.82 GHz. The Results From PIC-MCC Simulations and a Fluid Model With a Modified EEDF Are Provided as References

4.4 Plasma Shielding Effect

Air breakdown and plasma shielding triggered by geometry is demonstrated in this example. As shown in Figure 8a, the solution domain considered in this example is a parallel plate waveguide with a metallic wall placed between the two parallel plates, which forms a rectangular aperture (denoted in red in the figure). The solution domain is truncated from the left and the right using the ABC. A 25-GHz, 2.0-MV/m and vertically (the y direction) polarized plane wave with a tapered sinusoidal temporal profile is launched from the left boundary and propagates toward the right direction (the z direction). A 100-torr, 300-K air is assumed to be confined in the aperture area, with the rest of the domain filled with vacuum. The initial spatial profile of the electron density is set to be sinusoidal in both y and z directions, which reaches its maximum value of $10^{15}/m^3$ at the center of the aperture. Two observation points P1 ($x = y = 0.0$ mm, $z = 0.0$ mm) and P2 ($x = y = 0.0$ mm, $z = 2.81$ mm) are also shown in Figure 8a.

Besides the five-moment model presented in this report, this example has been simulated using a simplified diffusion model [14], where only the electron density and velocity were considered. It should be pointed out that in the diffusion model, the plasma parameters (ionization, attachment,

21

and momentum transfer frequencies, etc.) were obtained by empirical models based on measured data, which were nonlinear functions of the reduced effective electric field E_{eff}/P, whereas in the five-moment model, the plasma parameters are obtained by integrating collision cross sections with non-Maxwellian EEDF, which are nonlinear functions of the electron energy. As a result, these two models are very different in terms of the physical quantities under consideration, governing equations and plasma parameters calculation.

Shown in Figure 8b, Figure 8c and Figure 8e are the electric fields recorded at P1 and P2 and the electron density evolution recorded at P1. The comparisons are made between these two different models. Excellent agreements are achieved, which show that the physical quantities of interest can be obtained by very different physical models. Shown in Figure 8d is the comparison of electric fields recorded at P1 and P2. Apparently, after breakdown takes place at 0.5 ns, the incident fields are blocked and only a small portion of energy can transmit to the observation point P2. In Figure 8f, the electron energy and temperature at P1 with respect to time are given, which provide more physical insight of the process and fidelity of the simulation.

22
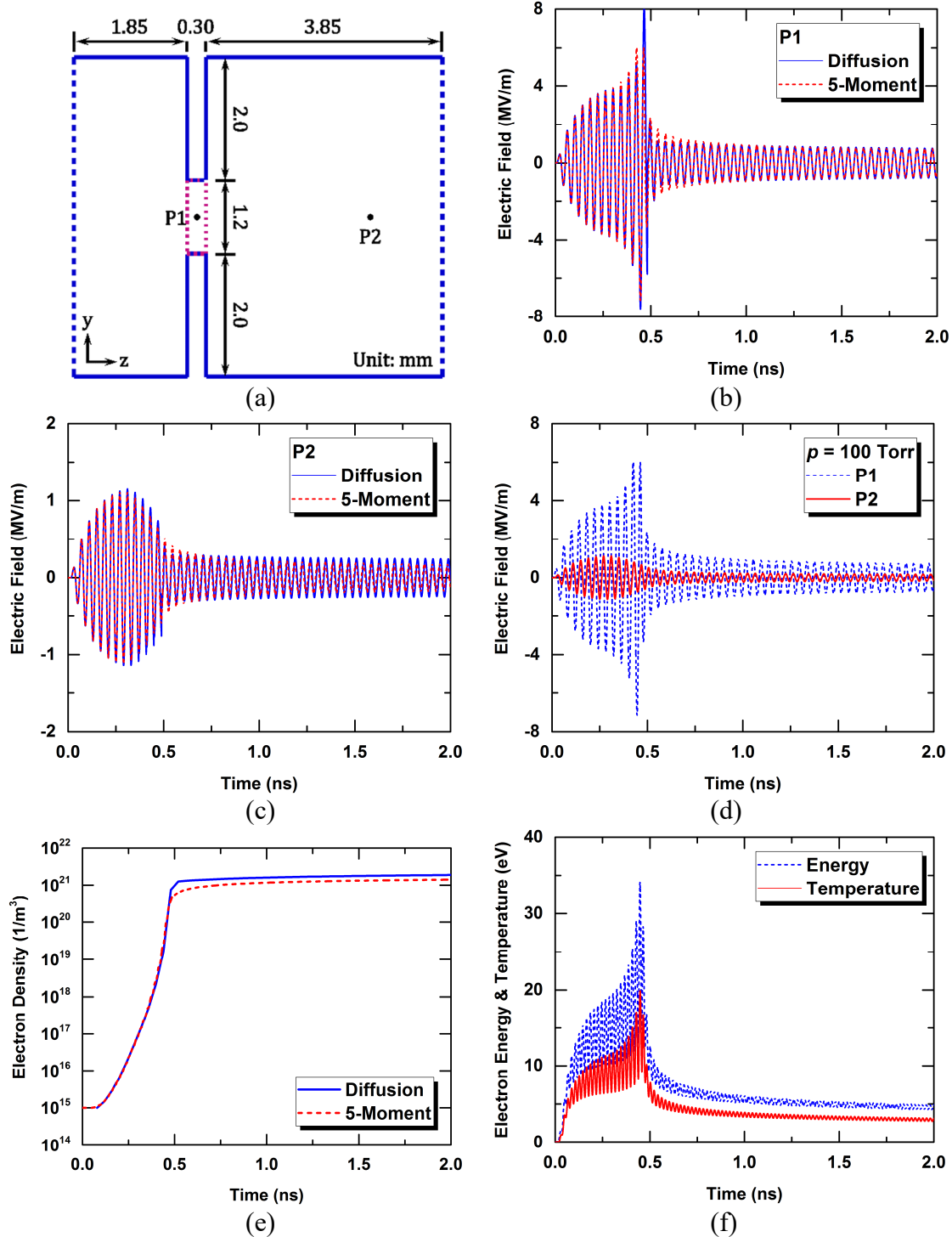
Figure 8. Microwave Breakdown and Plasma Shielding in a Metallic Aperture. (a) Illustration of the Solution Domain. (b) and (c) Comparison of the Electric Fields Simulated Using the Diffusion Model and the Five-Moment Model, Recorded at P1 and P2, Respectively. (d) Temporal Response of the Electric Fields Recorded at P1 and P2. (e) Temporal Evolution of the Electron Density Recorded at P1. (f) Temporal Evolution of the Electron Energy and Temperature Recorded at P1

23

4.5   Air Breakdown Around PEC Objects

As the last example, air breakdown around two perfectly electric conducting (PEC) cylinders are simulated using the five-moment model. This example is designed to demonstrate the plasma pattern formation and the scattering characteristic change after air breakdown. Here, two PEC cylinders with the same radius of 0.25 mm are placed in free space. A 5.5-MV/m, 200-GHz and y-polarized plane wave is incident from the z-direction. Shown in Figure 9 is the scattered electric field distribution when the entire simulation domain is filled with vacuum, which serves as the baseline for comparison. When the space is filled with 100-Torr, 300-K ambient air with $10^6/m^3$ initial electrons, the incident HPM triggers breakdown, first between the two PEC cylinders where the field is intensified. Due to the mutual couplings among the electromagnetic fields, the PEC scatterers and the plasma fluid, the ionized electrons follow a similar distribution as the scattered field pattern, as shown in Figure 10c, Figure 10e and Figure 10f. At 0.25 ns, although increased by 11 orders of magnitude, the electron density is still low, with a maximum density being $1.23\times10^{17}/m^3$. The electron oscillation does not contribute significantly to the scattered electric field. As a result, the electric fields presented in Figure 10a and Figure 10b are very similar to those given in Figure 9. As the breakdown process continues, the electron density and energy increase further. At 0.5 ns, the maximum electron density has increased by another 5 orders of magnitude, reaching as high as $5.92\times10^{22}/m^3$ (Figure 11c). The strong electron oscillation starts to alter the scattered field pattern. As can be seen in Figure 11a and Figure 11b, the scattered fields are significantly different from those recorded at 0.25 ns and those in the vacuum case. Due to the strong electron radiation, certain micro-patterns are formed in Figure 11, which have a characteristic length much smaller than the wavelength of the incident electromagnetic field. This is an illustration of the multiscale feature caused by the complicated electromagnetic--plasma interactions, which can only be captured by a numerical method with a high spatial resolution.

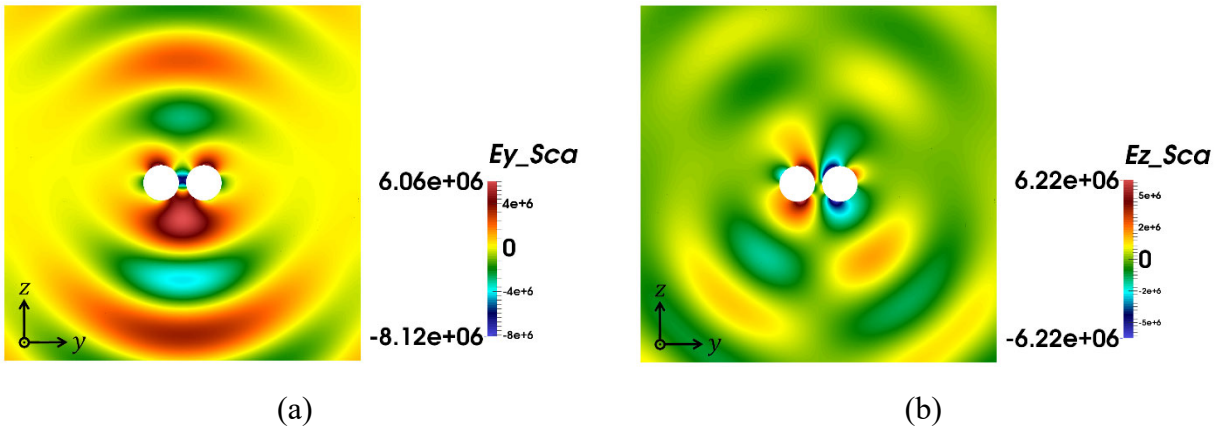(a)   (b)

Figure 9. Scattered Electric Field Distribution in Vacuum. (a) E_y; **(b)** E_z

24

Figure 10. Electric Field and Plasma Quantities Observed at 0.25 ns. (a) E_y**; (b)** E_z**; (c) Electron Density; (d) The Magnitude of the Electron Velocity; (e) Electron Energy and (f) Electron Temperature**
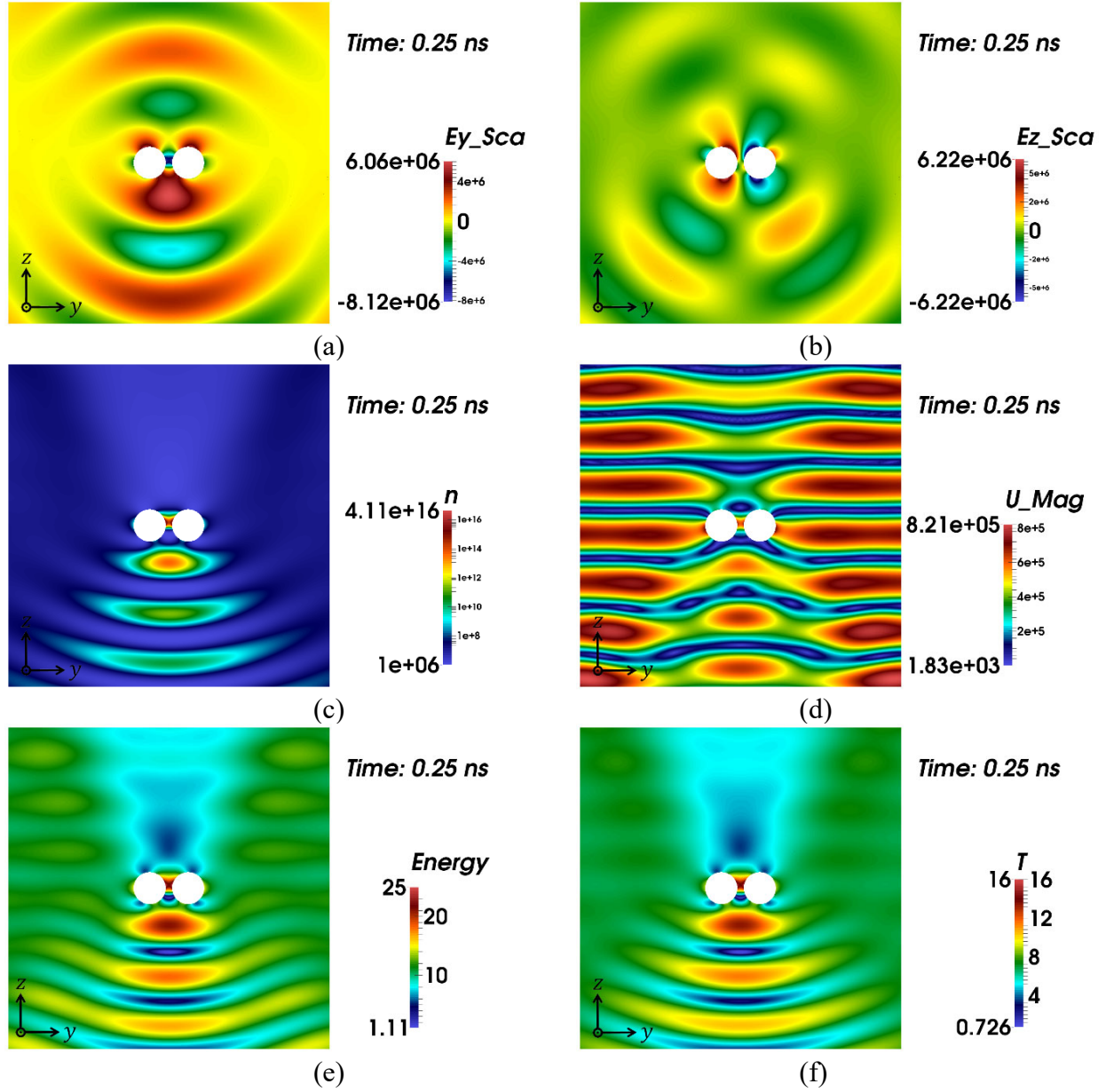
25
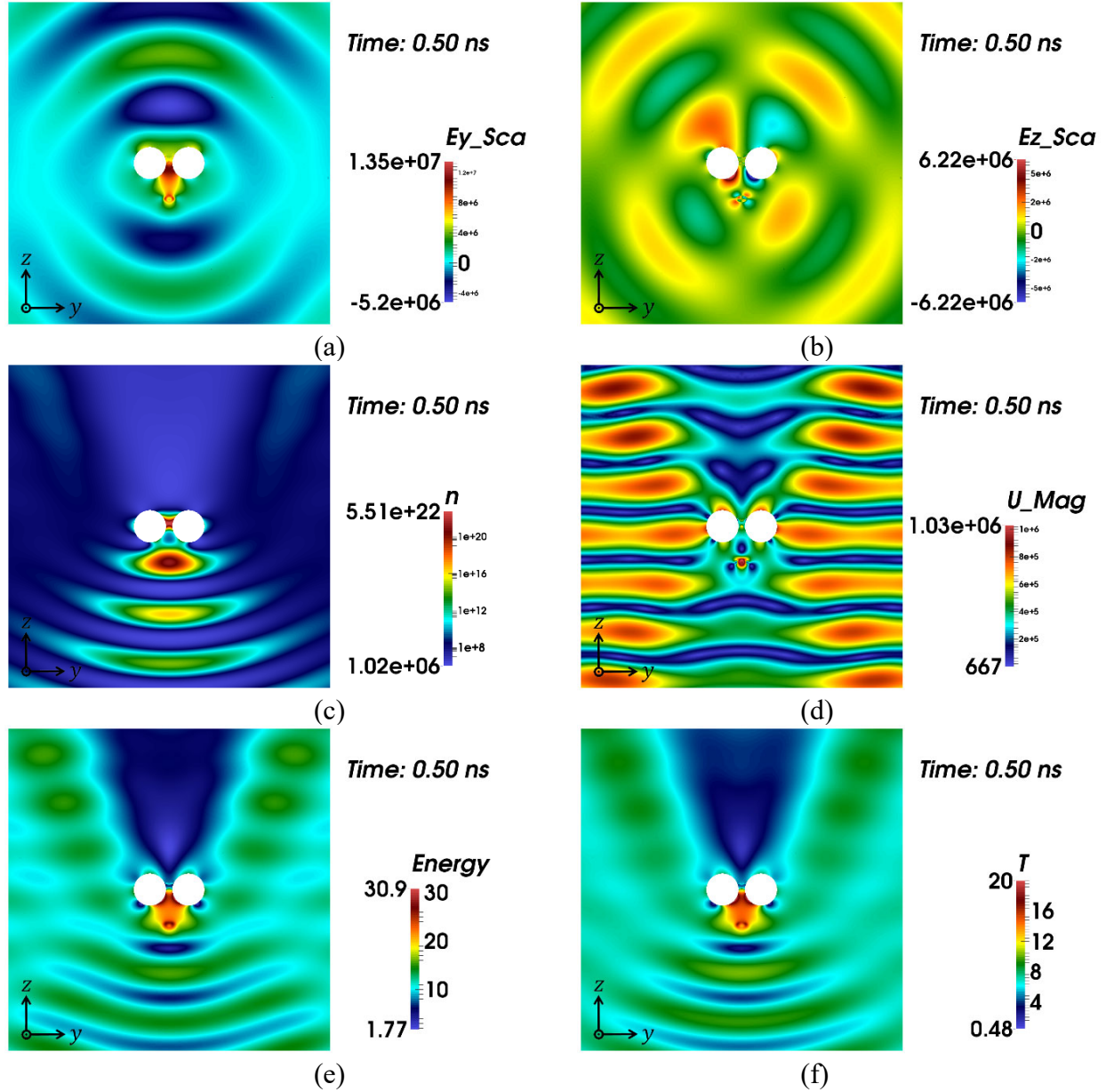
Figure 11. Electric Field and Plasma Quantities Observed at 0.5 ns. (a) E_y**; (b)** E_z**; (c) Electron Density; (d) The Magnitude of the Electron Velocity; (e) Electron Energy and (f) Electron Temperature**

To better understand the physical process, the plasma quantities and secondary fields are plotted along the z-axis in Figure 12. As shown in Figure 12a, the electron density follows the scattered wave pattern in the lit region ($z < 0$ mm). At 0.25 ns, the electron energy has a highest peak at around $z = 0$ mm (Figure 12b), which leads to the fastest increase of the electron density in this region. When its density reaches $10^{22}/m^3$ at 0.5 ns, the electrons start to shield the electromagnetic field. This results in a strong reflection of the field and leads to a higher energy peak at around $z = -0.6$mm, which will cause a stronger ionization and faster increase of the electron density in that region. When this process continues, density spikes will gradually form

26

and propagate toward the source of the incident field. This phenomenon is presented in Figure 13 and Figure 14 in two and one dimension, respectively, where the process of the plasma pattern formation can be observed very clearly. Such a filamentary plasma array formation was also observed in experiments [3]-[5], in which a similar plasma pattern has been recorded by a high-speed camera. From these two figures, the propagation velocity of the plasma filaments can be estimated to be about 1500 km/s, which is on the same order of the theoretic estimation of $2\sqrt{D_e \nu_i}$ [6] where D_e and ν_i are the free electron diffusion and the ionization coefficients, respectively. From Figure 15, the spacing between two adjacent filaments can be seen very clearly, which is about a quarter wavelength $\lambda_0/4 = 0.375$ mm in free space. This is because the strong field reflection from the filaments results in a standing wave pattern in the lit region, which generates plasma filaments with a similar standing wave pattern.
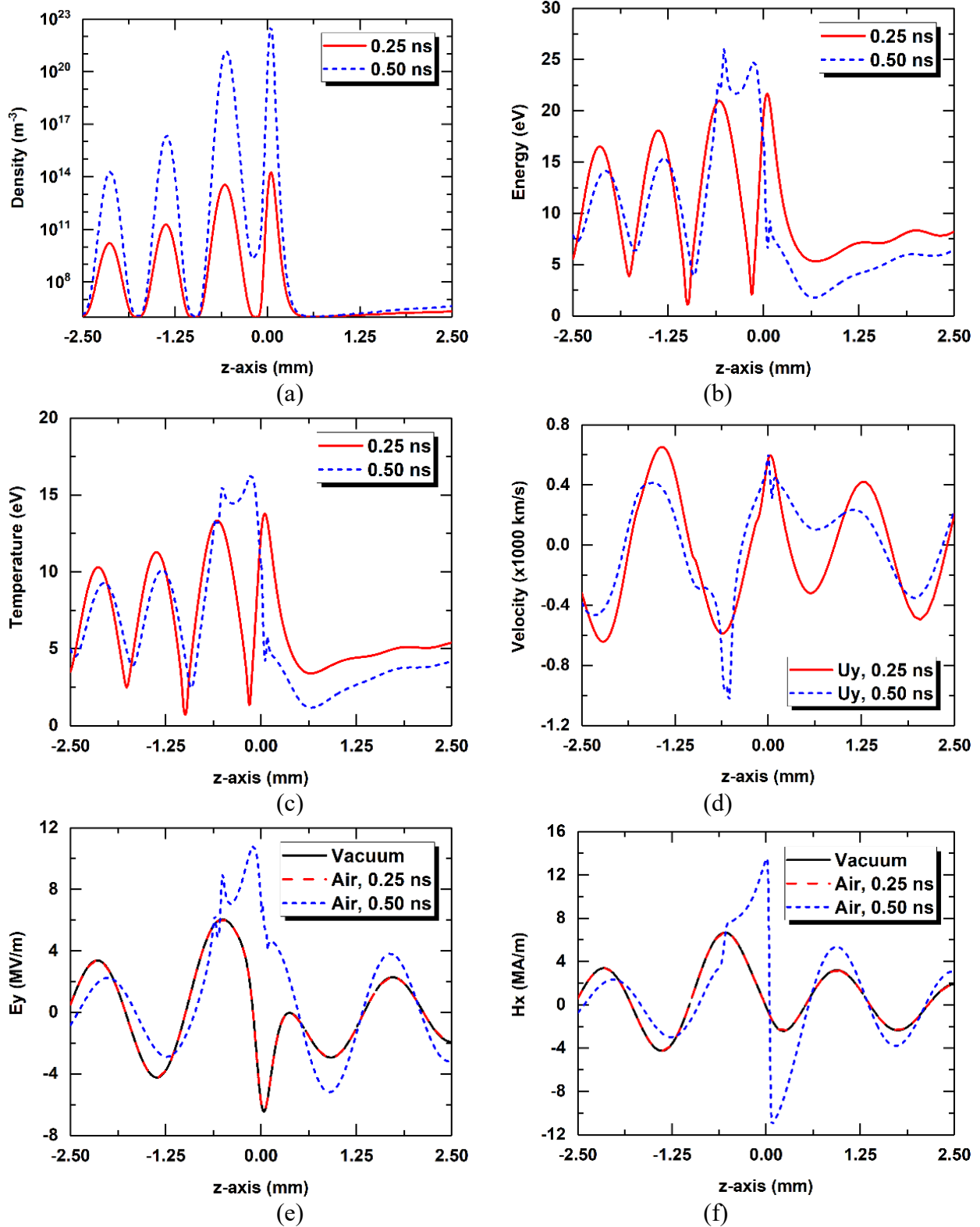
Figure 12. Comparisons of Plasma Quantities and the Secondary Electromagnetic Fields Observed at 0.25 and 0.50 ns Along the *z*-Axis. (a) Electron Density; (b) Electron Energy; (c) Electron Temperature; (d) Electron Velocity U_y; (e) Electric Field E_y and (f) Magnetic Field H_x

28
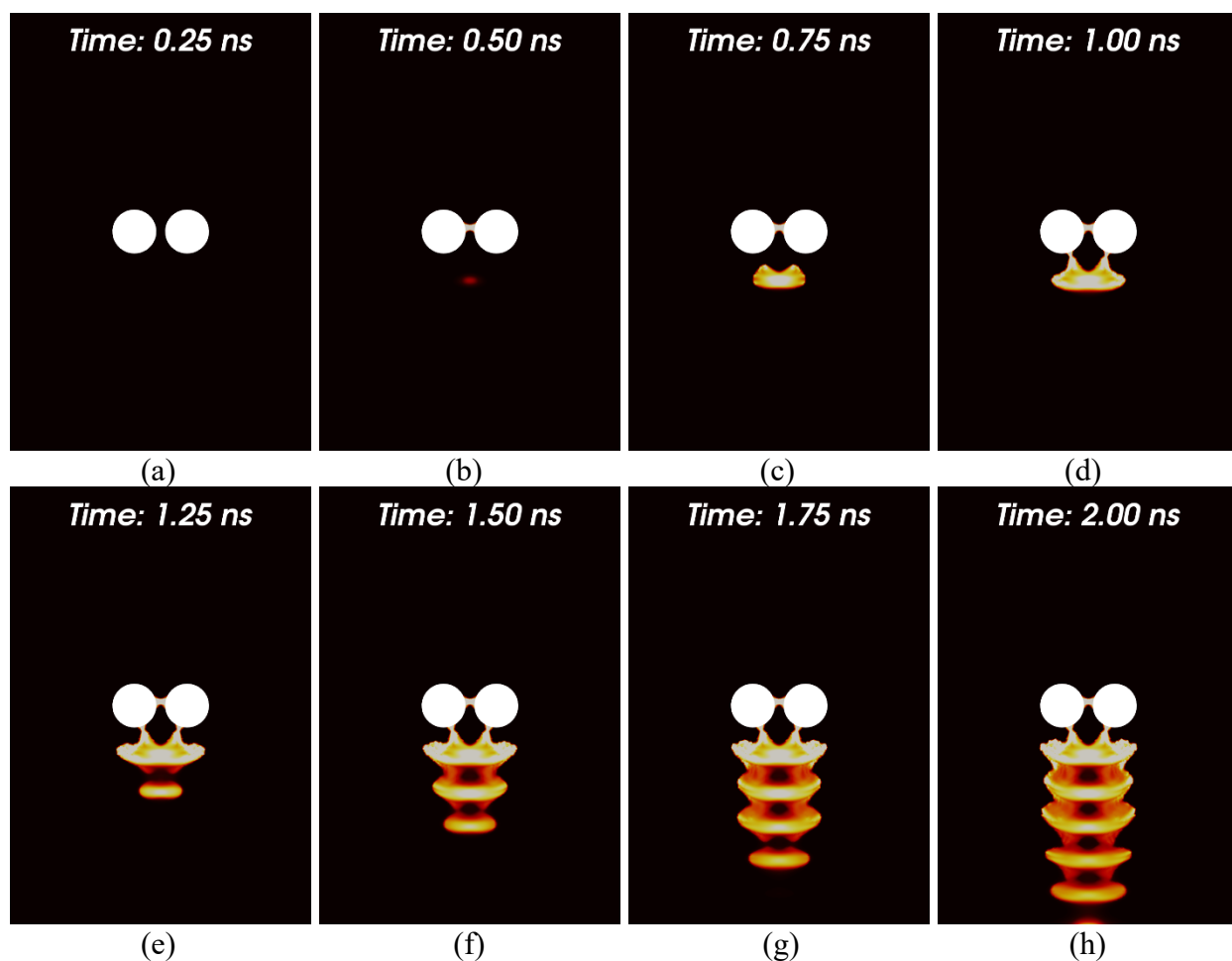
Figure 13. Electron Density Distribution in Linear Scale, Observed at (a) 0.25 ns; (b) 0.50 ns; (c) 0.75 ns; (d) 1.00 ns; (e) 1.25 ns; (f) 1.50 ns; (g) 1.75 ns; and h) 2.00 ns

29

Figure 14. Electron Density Distribution Along the *z*-Axis, in Linear Scale, Observed at Different Time Instants

(a)   (b)

Figure 15. Spacing of the Plasma Filaments. (a) 2D Plot; (b) 1D Plot

30

It is shown in this section that this very interesting and highly complicated physical phenomenon can be reproduced successfully with the proposed numerical method, through which many physical details can be revealed.

5.0 CONCLUSIONS

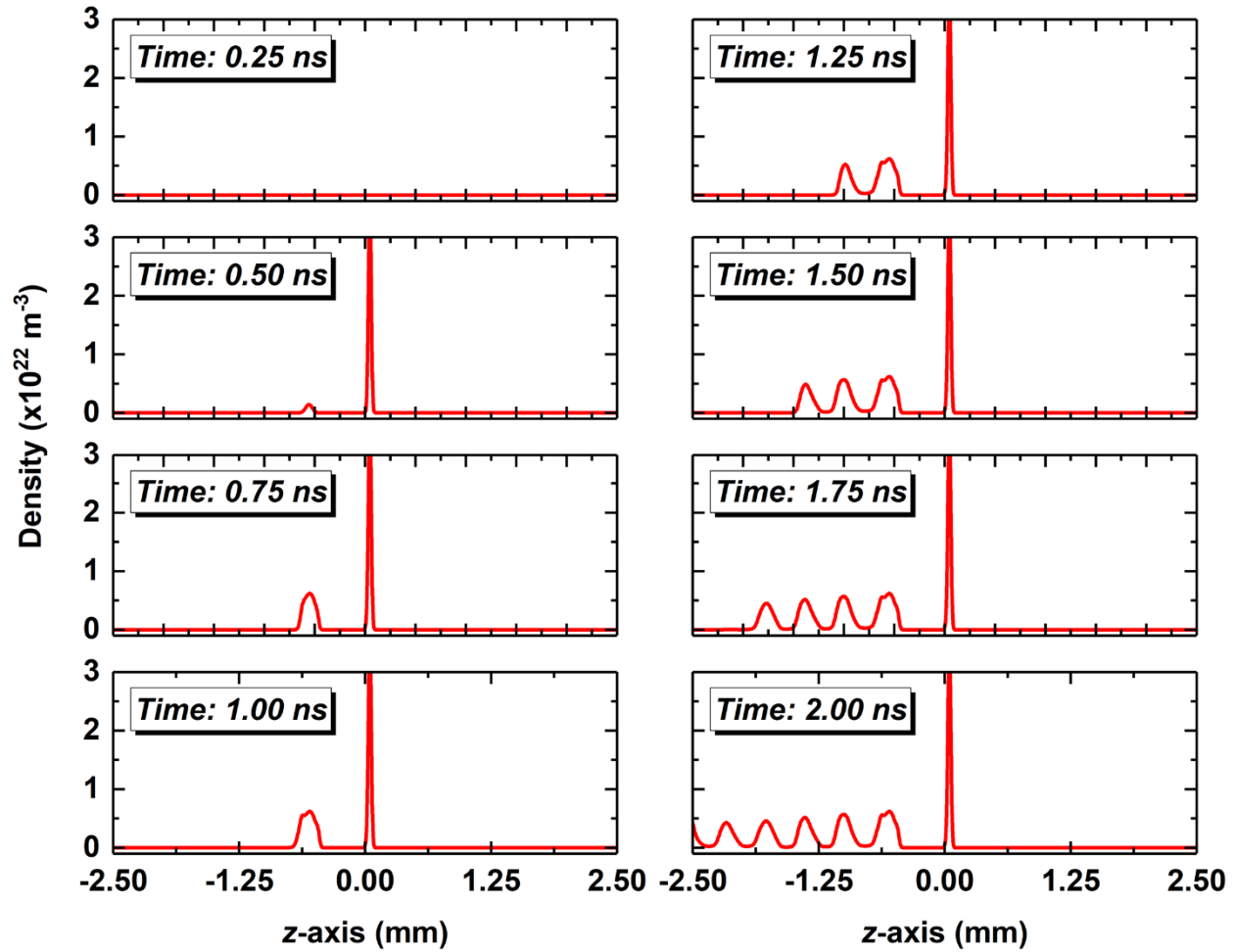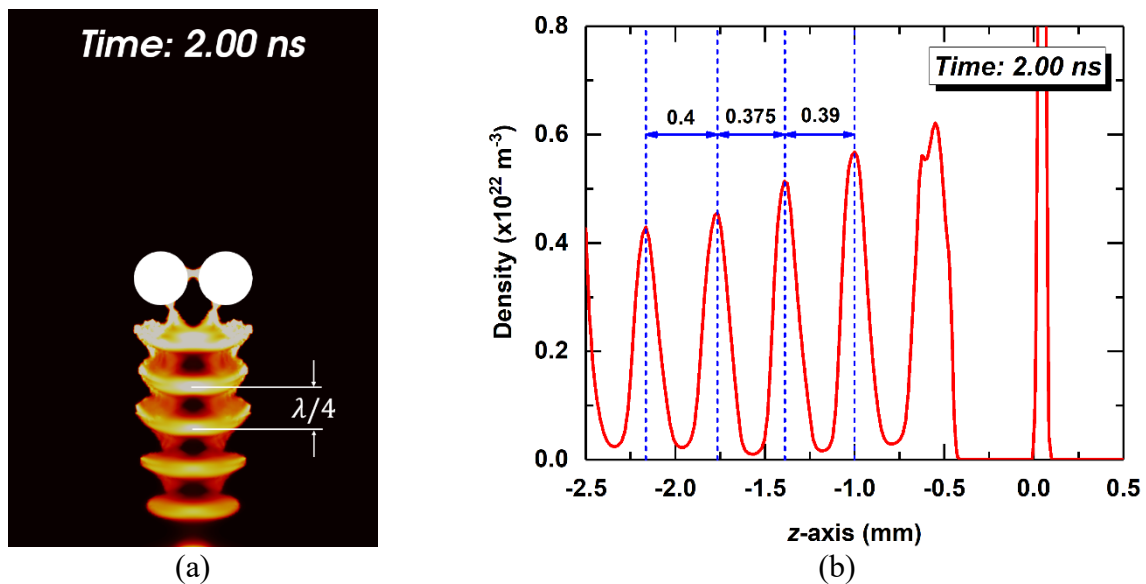In this report, the five-moment plasma fluid model has been employed to develop a DGTD-based simulation of the HPM breakdown in air, which is able to provide more physical insight with a higher fidelity compared to simpler models. To characterize of the highly non-equilibrium breakdown process, the transport coefficients are calculated using the non-Maxwellian EEDFs solved from the BOLSIG+ package. The self-consistent Maxwell--Euler system equations have been solved using a coupled DGTD method, where the upwind flux is used for Maxwell's equations and the Lax-Friedrichs flux is used for Euler's equations. The employment of the DGTD method with higher-order nodal basis functions provides a sufficient spatial resolution to capture the fast-varying micro-patterns of the electromagnetic fields and the plasma fluids. Several numerical examples have been presented to show the difference between the use of the Maxwellian and non-Maxwellian EEDFs, illustrate the air breakdown behavior under different ambient pressures, and demonstrate the plasma formation and electromagnetic shielding phenomena. With the method presented in this report, many interesting physical phenomena can be modeled and simulated with a high fidelity.

6.0 REFERENCES

[1]   W. Woo and J. S. DeGroot, "Microwave absorption and plasma heating due to microwave breakdown in the atmosphere," *Phys. Fluids*, vol. 27, no. 2, pp. 475–487, Feb. 1984.

[2]   J. H. Yee, D. J. Mayhall, G. E. Sieger, and R. A. Alvarez, "Propagation of intense microwave pulses in air and in a waveguide," *IEEE Trans. Antennas Propag.*, vol. 39, no. 9, pp. 1421–1426, 1991.

[3]   Y. Hidaka, E. M. Choi, I. Mastovsky, M. A. Shapiro, J. R. Sirigiri, and R. J. Temkin, "Observation of large arrays of plasma filaments in air breakdown by 1.5-MW 110-GHz gyrotron pulses," *Phys. Rev. Lett.*, vol. 100, pp. 035003–1–035003–4, Jan. 2008.

[4]   Y. Hidaka, E. M. Choi, I. Mastovsky, M. A. Shapiro, J. R. Sirigiri, R. J. Temkin, G. F. Edmiston, A. A. Neuber, and Y. Oda, "Plasma structures observed in gas breakdown using a 1.5 MW, 110 GHz pulsed gyrotron," *Phys. Plasmas*, vol. 16, pp. 055702–1–055702–7, 2009.

[5]   S. K. Nam and J. P. Verboncoeur, "Theory of filamentary plasma array formation in microwave breakdown at near-atmospheric pressure," *Phys. Rev. Lett.*, vol. 103, pp. 055004–1–055004–4, Jul. 2009.

[6]   J. P. Boeuf, B. Chaudhury, and G. Q. Zhu, "Theory and modelling of self-organization and propagation of filamentary plasma arrays in microwave breakdown at atmospheric pressure," *Phys. Rev. Lett.*, vol. 104, pp. 015002–1–015002–4, 2010.

[7]   B. Chaudhury and J. P. Boeuf, "Computational studies of filamentary pattern formation in a high power microwave breakdown generated air plasma," *IEEE Trans. Plasma Sci.*, vol. 38, pp. 2281–2288, 2010.

[8]   B. Chaudhury, J. P. Boeuf, and G. Q. Zhu, "Pattern formation and propagation during microwave breakdown," *Phys. Plasmas*, vol. 17, pp. 123505–1–123505–11, 2010.

[9]   P. Zhao, C. Liao, W. Lin, L. Chang, and H. Fu, "Numerical studies of the high power microwave breakdown in gas using the fluid model with a modified electron energy distribution function," *Phys. Plasmas*, vol. 18, pp. 102111–1–102111–6, 2011.

[10] A. Hamiaz, R. Klein, X. Ferrieres, O. Pascal, J. P. Boeuf, and J. R. Poirier, "Finite volume time domain modelling of microwave breakdown and plasma formation in a metallic aperture," *Comput. Phys. Commun.*, vol. 183, pp. 1634–1640, 2012.

[11] K. Kourtzanidis, F. Rogier, and J.-P. Boeuf, "ADI-FDTD modeling of microwave plasma discharges in air towards fully three-dimensional simulations," *Comput. Phys. Commun.*, vol. 195, pp. 49–60, Oct. 2015.

[12] S. Yan and J.-M. Jin, "Three-dimensional time-domain finite-element simulation of dielectric breakdown based on nonlinear conductivity model," *IEEE Trans. Antennas Propag.*, vol. 64, no. 7, pp. 3018–3026, Jul. 2016.

[13] S. Yan and J.-M. Jin, "A fully coupled nonlinear scheme for time-domain modeling of high-power microwave air breakdown," *IEEE Trans. Microw. Theory Techn.*, vol. 64, no. 9, pp. 2718–2729, Sep. 2016.

[14] S. Yan, A. D. Greenwood, and J.-M. Jin, "Modeling of plasma formation during high-power microwave breakdown in air using the discontinuous Galerkin time-domain method (invited paper)," *IEEE J. Multiscale and Multiphys. Comput. Techn.*, vol. 1, pp. 2–13, Jun. 2016.

[15] G. J. M. Hagelaar and L. C. Pitchford, "Solving the Boltzmann equation to obtain electron transport coefficients and rate coefficients for fluid models," *Plasma Sources Sci. Technol.*, vol. 14, no. 4, pp. 722–733, Oct. 2005.

[16] K. S. Yee, J. S. Chen, and A. H. Chang, "Conformal finite-difference time-domain (FDTD) with overlapping grids," *IEEE Trans. Antennas Propag.*, vol. 40, no. 2, pp. 1068–1075, 1992.

[17] B. Cockburn and C.-W. Shu, "The Runge-Kutta discontinuous Galerkin finite element method for conservation laws V: Multidimensional systems," *J. Comput. Phys.*, vol. 141, pp. 199–224, 1998.

[18] J. S. Hesthaven and T. Warburton, *Nodal Discontinuous Galerkin Methods: Algorithms, Analysis, and Applications.* New York: Springer, 2008.

[19] S. D. Gedney, C. Luo, J. A. Roden, R. D. Crawford, B. Guernsey, J. A. Miller, T. Kramer, and E. W. Lucas, "The discontinuous Galerkin finite-element time-domain method solution of Maxwell's equations," *Applied Comput. Electromag. Society J.*, vol. 24, no. 2, pp. 129–142, Apr. 2009.

[20] L. D. Angulo, J. Alvarez, M. F. Pantoja, S. G. Garcia, and A. R. Bretones, "Discontinuous Galerkin time domain methods in computational electrodynamics: State of the art," *FERMAT: Forum for Electromagnetic Research Methods and Application Technologies*, vol. 10, pp. 1–24, Aug. 2015.

[21] S. Descombes, C. Durochat, S. Lanteri, L. Moya, C. Scheid, and J. Viquerat, "Recent advances on a DGTD method for time-domain electromagnetics," *Photonics and Nanostructures Fundamentals and Applications*, vol. 11, pp. 291–302, 2013.

[22] S. Yan and J.-M. Jin, "A continuity-preserving and divergence-cleaning algorithm based on purely and damped hyperbolic Maxwell equations in inhomogeneous media," *J. Comput. Phys.*, vol. 334, pp. 392–418, Apr. 2017.

[23] S. Yan, C.-P. Lin, R. R. Arslanbekov, V. I. Kolobov, and J.-M. Jin, "A discontinuous Galerkin time-domain method with dynamically adaptive Cartesian meshes for computational electromagnetics," *IEEE Trans. Antennas Propag.*, vol. 65, no. 6, pp. 3122–3133, Jun. 2017.

[24] S. Yan and J.-M. Jin, "A dynamic p-adaptive DGTD algorithm for electromagnetic and multiphysics simulations," *IEEE Trans. Antennas Propag.*, vol. 65, no. 5, pp. 2446–2459, May 2017.

[25] J. Guan, S. Yan, and J.-M. Jin, "An openMP-CUDA implementation of multilevel fast multipole algorithm for electromagnetic simulation on multi-GPU computing systems," *IEEE Trans. Antennas Propag.*, vol. 61, no. 7, pp. 3607–3616, Jul. 2013.

[26] J. Guan, S. Yan, and J.-M. Jin, "An accurate and efficient finite element-boundary integral method with GPU acceleration for 3-D electromagnetic analysis," *IEEE Trans. Antennas Propag.*, vol. 62, no. 12, pp. 6325–6336, Dec. 2014.

[27] J. A. Bittencourt, *Fundamentals of Plasma Physics.* New York: Springer-Verlag, 2004.

[28] C. K. Birdsall and A. B. Langdon, *Plasma Physics via Computer Simulation.* New York: Taylor & Francis, 2005.

[29] P. M. Bellan, *Fundamentals of Plasma Physics.* Cambridge: Cambridge University Press, 2006.

[30] S. Jardin, *Computational Methods in Plasma Physics.* Boca Raton, FL: CRC Press, 2010.

[31] S. A. Lawton and A. V. Phelps, "Excitation of the $b^1\Sigma_g^+$ state of O_2 by low energy electrons," *J. Chem. Phys.*, vol. 69, no. 3, pp. 1055–1068, Aug. 1978.

[32] PHELPS database. [Online]. Available: http://www.lxcat.laplace.univ-tlse.fr

[33] A. V. Phelps and L. C. Pitchford, "Anisotropic scattering of electrons by N_2 and its effect on electron transport," *Phys. Rev. A*, vol. 31, no. 5, pp. 2932–2949, May 1985.

[34] SIGLO database. [Online]. Available: http://www.lxcat.laplace.univ-tlse.fr

[35] J. C. Butcher, *Numerical Methods for Ordinary Differential Equations.* New York: Wiley, 2003.

[36] S. Gottlieb, D. Ketcheson, and C.-W. Shu, *Strong Stability Preserving Runge-Kutta and Multistep Time Discretizations.* Hackensack, NJ: World Scientific, 2011.

[37] G. Wu, "Shape properties of pulses described by double exponential function and its modified forms," *IEEE Trans. Electromagn. Compat.*, vol. 56, no. 4, pp. 923–931, Aug. 2014.

[38] S. Yan, A. D. Greenwood, and J.-M. Jin, "DGTD simulation of HPM air breakdown using a 5-moment fluid model and non-Maxwellian EEDF," in *Proc. IEEE Antennas Propag. Symp.*, San Diego, CA, USA, July 2017.

[39] H. C. Kim and J. P. Verboncoeur, "Transition of window breakdown from vacuum multipactor discharge to RF plasma," *Phys. Plasmas*, vol. 13, pp. 123506–1–123506–5, 2006.

[40] J. P. Verboncoeur, "Particle simulation of plasmas: Review and advances," *Plasma Phys. Control. Fusion*, vol. 47, pp. A231–A260, 2005.

LIST OF SYMBOLS, ABBREVIATIONS AND ACRONYMS

$\boldsymbol{B}^{\text{inc}}$	magnetic flux of the incident high-power pulse
$\mathfrak{D}$	material parameter tensor
D_{e}	free electron diffusion coefficient
DEXP	difference of double exponentials
DGTD	discontinuous Galerkin time-domain
$\mathcal{E}$	mean energy
$\boldsymbol{E}$	electric field
EEDF	electron energy distribution function
E_{eff}/P	reduced effective electric field
$\boldsymbol{E}^{\text{inc}}$	electric field of the incident high-power pulse
$\mathfrak{F}$	physical flux tensor
$\boldsymbol{F}$	Lorentz force
F_0	EEDF
FDTD	finite-difference time-domain
FETD	finite-element time-domain
f	electron distribution function
$\boldsymbol{G}$	conservative variables (unknown quantity vector)
GPU	graphic processing unit
$\boldsymbol{H}$	magnetic field
HPM	high-power microwave
$\mathbb{I}$	identity tensor
k_{B}	Boltzmann constant
LHS	left-hand side
l_i	testing function
M_k	mass of the target gas species of collision process k
m_{e}	electron mass at rest
N_{Air}	number density of the ambient air
n	particle density
$\mathbb{P}$	pressure tensor
P	scalar pressure
PEC	perfectly electric conducting
PIC-MCC	particle-in-cell with Monte-Carlo collision
$\boldsymbol{Q}$	heat flux vector
Q_{e}	electron energy loss frequency
q_{e}	electron charge
RHS	right-hand side
$\boldsymbol{r} = (x, y, z)$	physical space
$\boldsymbol{S}$	source term of conservation equations
T	temperature
$\boldsymbol{U}$	mean velocity
V_e	tetrahedral element
$\boldsymbol{v} = (v_x, v_y, v_z)$	velocity space
x_k	mole fraction of the target gas species of collision process k

ε_k	threshold energy
ϵ	permittivity of the medium
Φ	macroscopically averaged quantity
γ	ratio of specific heats
λ	characteristic velocity
λ_0	wavelength in free space
μ	permeability of the medium
ν_a	attachment frequency
ν_c	total collision frequency
ν_i	ionization frequency
σ_k	cross section of collision process k
$(\mathfrak{F}^* - \mathfrak{F}) \cdot \hat{\boldsymbol{n}}$	total flux
$\langle \cdot \rangle$	addition function
$[\![\cdot]\!]$	jump function

DISTRIBUTION LIST

DTIC/OCP
8725 John J. Kingman Rd, Suite 0944
Ft Belvoir, VA 22060-6218   1 cy

AFRL/RVIL
Kirtland AFB, NM 87117-5776   1 cy

Official Record Copy
AFRL/RDHE/Andrew Greenwood   1 cy